Journal of Materials Chemistry A

REVIEW

View Article Online
View Journal | View Issue

Published on 21 October 2014. Downloaded by ENEA - CASSACCIA on 12/06/2016 17:53:20.

Cite this: J. Mater. Chem. A, 2015, 3, 8926

Halide perovskite materials for solar cells: a theoretical review

Wan-Jian Yin,*[ab] Ji-Hui Yang,[a] Joongoo Kang,[a] Yanfa Yan[b] and Su-Huai Wei*[a]

Received 23rd September 2014
Accepted 21st October 2014

DOI: 10.1039/c4ta05033a

www.rsc.org/MaterialsA

Halide perovskites have recently emerged as promising materials for low-cost, high-efficiency solar cells. The efficiency of perovskite-based solar cells has increased rapidly, from 3.8% in 2009 to 19.3% in 2014, by using the all-solid-state thin-film architecture and engineering cell structures with mixed-halide perovskites. The emergence of perovskite solar cells revolutionized the field not only because of their rapidly increased efficiency, but also flexibility in material growth and architecture. The superior performance of the perovskite solar cells suggested that perovskite materials possess intrinsically unique properties. In this review, we summarize recent theoretical investigations into the structural, electrical, and optical properties of halide perovskite materials in relation to their applications in solar cells. We also discuss some current challenges of using perovskites in solar cells, along with possible theoretical solutions.

Introduction

Perovskites generally refer to a class of oxides with chemical formula ABO_3 that exhibit sought-after physical properties such as magnetic, ferroelectric, and two-dimensional electronic conductivity.[1,2] Recently, halide perovskites have drawn substantial interest in the fields of material research, as well as chemistry and physics.[3–15] This is due to the high efficiency of solid-state solar cells based on halide perovskites, which reached 17.9% in 2014,[16] up from 9.7% in 2012.[17] For comparison, liquid-electrolyte solar cells had an efficiency of 3.8% in 2009.[11]

Research into halide perovskites with chemical formula (A = 1 + ions or molecules, B = Ge, Sn, Pb, and X = I, Br, Cl) has existed for more than a century.[18] Their crystal structures as well as ferroelectric behaviors were initially investigated about half a century ago.[19–25] However, the electricity-to-light conversion ability of halide perovskites, applied to light-emitting diodes (LEDs), was initially discovered by Mitzi's group in the 1990s[26–29] and such LEDs have only recently been fabricated.[30] Although the light-to-electricity conversion (photovoltaic) process is the reverse of the electricity-to-light process, the first published report of using halide perovskites as solar cell absorbers emerged almost two decades later.[11]

In 2009 and 2006, Miyasaka *et al.*[11,31] used organometallic perovskites $CH_3NH_3PbI_3$ and $CH_3NH_3PbBr_3$ in dye-sensitized solar cells (DSSCs) and achieved efficiencies of 3.8% and 2.6%, respectively. By using $CH_3NH_3PbI_3$ nanoparticles and TiO_2

[a]National Renewable Energy Laboratory, Golden, CO 80401, USA. E-mail: wan-jian.yin@nrel.gov; suhuai.wei@nrel.gov
[b]Department of Physics and Astronomy, University of Toledo, OH 43606, USA

Wan-Jian Yin received his B.S. in Physics (2004) and Ph.D. in Theoretical Physics (2009) from Fudan University, China. He joined the National Renewable Energy Laboratory (NREL) as a postdoctoral researcher in 2009. He is currently holding a joint position of research associate in NREL and research assistant professor in The University of Toledo. His research interests include energy-related materials and defect physics in semiconductors.

Ji-Hui Yang received his B.S. in Physics in 2008 and Ph.D. in 2013 from Fudan University. He is currently a Postdoc at the National Renewable Energy Laboratory. His research is mainly focused on photovoltaic materials and multiferroic materials, including material search and design, property studies and related theory development.

This journal is © The Royal Society of Chemistry 2015

Published on 21 October 2014. Downloaded by ENEA - CASSACCIA on 12/06/2016 17:53:20.

surface treatments, Park *et al.* achieved an efficiency of 6.5% in 2011,[32] creating a cell architecture similar to the extremely thin absorber (ETA) DSSC. In 2012, due to the corrosion problems associated with liquid electrolytes, Park and Grätzel *et al.* replaced the liquid-based hole transport layer with solid-state spiro-MeOTAD and immersed perovskites into the TiO_2 scaffold. Unexpectedly, this increased the efficiency to 9.7%.[17] Using a similar mesoscopic-structure architecture, Lee and Snaith *et al.* achieved an efficiency of 7.6%.[9] They further found that the efficiency could be boosted to 10.9% when replacing electrically conducting TiO_2 with electrically inert Al_2O_3. Although there are still uncertainties related to the claim that Al_2O_3 performs better than TiO_2, this finding indicated that perovskite itself might have efficient electrical transport properties. Following this clue, Liu and Snaith *et al.*[7] created efficient planar heterojunction perovskite solar cells using vapor deposition. The solar cell had no electron conductor scaffold other than a compact TiO_2 layer, similar to thin-film solar cells. An efficiency of 15.4% was achieved with this architecture. Recently, Seok *et al.*[33] combined planar and scaffold layers of mixed-halide $CH_3NH_3Pb(I_{1-x}Br_x)_3$, and through fine-tuning the thickness ratio of planar and scaffold layers as well as chemical compositions, they achieved consecutive record efficiencies from 16.2% to 17.9%.[16] Other developments include tuning perovskite properties with chemical compositions,[34,35] developing efficient growth methods,[33,36,37] optimizing hole transport materials,[38–40] and engineering interface properties.[41,42]

The superior performance of halide perovskite-based solar cells is reflected in their high open circuit voltage (V_{oc}). According to detailed balance theory,[43] the maximum V_{oc} ($V_{oc\text{-}max}$) of a semiconductor absorber is approximately its bandgap energy (E_g) subtracted by 0.25 eV. The ratio of $V_{oc\text{-}max}/E_g$ indicates how well the material will perform as a solar cell absorber. Table 1 lists record values for perovskite-based solar cells, with comparisons to several conventional solar cell absorbers. It is surprising that in terms of $V_{oc\text{-}max}/E_g$, perovskite-based solar cells are comparable to $Cu(In,Ga)Se_2$ (CIGS) and superior to CdTe and $Cu_2ZnSn(S,Se)_4$ (CZTSS) based solar cells.

Although theoretical investigations have not kept pace with experiments on halide perovskites, the basic electronic structures of halide perovskites were studied by first-principles calculations before the first perovskite solar cell was reported experimentally. First-principles calculation based on density functional theory (DFT) is a computational modelling method used to investigate the electronic structure of many-body systems. With this theory, the properties of a many-electron system can be determined by using density functionals, in which the exchange–correlation functional is the only not-well-defined. Therefore, different approximations of exchange–correlation functionals are used and may derive different results. Chang *et al.*[44] used local density approximation (LDA) to study cubic phase $CsPbX_3$ and $CH_3NH_3PbX_3$ (X = I, Br, Cl), and found that the hole effective mass was lighter than the electron effective mass, which was not the case in conventional semiconductors. Borriello *et al.*[45] used generalized gradient approximation (GGA) to study organic and inorganic perovskites based on tin halide and found that the stability against the distortion of the perovskite cage strongly depends on the embedded cation. Recently, due to experimental progress, many

Joongoo Kang received his B.S. in 2001, M.S. in 2003, and Ph.D. in 2007, all in Physics from KAIST, South Korea. He joined the National Renewable Energy Laboratory (NREL) in 2008, and he is currently a Senior Scientist at NREL. His research areas of interest include electronic structure theory of materials, design of advanced energy materials, and computational quantum physics.

Yanfa Yan has held the Ohio Research Scholar Chair in the Department of Physics and Astronomy at The University of Toledo, USA since 2011 and is a faculty member in the Ohio's Wright Center for Photovoltaics Innovation and Commercialization (PVIC). Previously, he was a Principal Scientist at the National Renewable Energy Laboratory (NREL), USA. Dr Yan's expertise includes theoretical study of electronic properties and defect physics of semiconductors and nanoscale characterization of microstructures, interfaces, and defects in thin-film photovoltaic materials. Dr Yan is a Fellow of the American Physical Society.

Su-Huai Wei received his B.S. in Physics from Fudan University in 1981 and Ph.D. from the College of William and Mary in 1985. He is currently a Principal Scientist at the National Renewable Energy Laboratory. His research is focused on developing electronic structure theory of materials, especially for semiconductors, oxides, and low-dimensional materials for energy related applications. He has published more than 380 papers in leading scientific journals, including more than 67 in Physical Review Letters with an H index of 83. He is a Fellow of both the American Physical Society and the Materials Research Society.

Published on 21 October 2014. Downloaded by ENEA - CASSACCIA on 12/06/2016 17:53:20.

Table 1 The room temperature bandgaps (E_g), open-circuit voltage (V_{oc}), short-circuit current (J_{sc}), fill factor (FF) and efficiency (η) of GaAs-, CIGS-, CdTe-, CZTSS-, and $CH_3NH_3PbI_3$-based solar cells. Both the experimentally achieved and theoretical maximum values by the Shockley–Queisser limit are shown for comparison

	E_g (eV)		V_{oc} (V)	$V_{oc}/V_{oc\text{-}max}$	J_{sc} (mA cm^{-2})	$J_{sc}/J_{sc\text{-}max}$	FF (%)	FF/FF$_{max}$	η (%)
GaAs	1.43	Exp	1.12	95.7%	29.68	94.0%	86.5	96.6%	28.8
		SQ-limit	1.17		31.56		89.5		33.0
CIGS	1.14	Exp	0.752	83.9%	35.3	82.5%	77.2	88.5%	20.5
		SQ-limit	0.896		42.81		87.2		33.5
CdTe	1.44	Exp	0.872	73.9%	29.47	94.6%	79.5	88.7%	20.4
		SQ-limit	1.18		31.16		89.6		32.8
CZTSS	1.13	Exp	0.513	57.8%	35.2	81.3%	69.8	80.1%	12.6
		SQ-limit	0.887		43.3		87.1		33.4
$CH_3NH_3PbI_{3-x}Cl_x$	1.55	Exp	1.13	88.3%	22.75	83.6%	75.0	83.2%	15.4
		SQ-limit	1.28		27.20		90.2		31.4

theoretical investigations on structural and electronic properties of halide perovskites are emerging.[46–71] Different methodologies have been adopted, using exchange–correlation functionals such as LDA, GGA, hybrid functional methods (HSE), and quasiparticle GW methods. Other options include spin–orbit-coupling (SOC) and van der Waals interactions.

In this review, we summarize our recent theoretical investigations on halide perovskites[62,63,67,70] and provide comparisons with existing theoretical and experimental work. The unique properties of halide perovskites were systematically investigated and explained as the origin of high performance in perovskite-based solar cells.[62] The dominating defects in halide perovskites were found not to be harmful because they do not create a detrimental deep level within the bandgap,[63,72] which could be carrier traps and recombination centers for electron–hole in solar cells. We also discuss how the stability and performance of perovskite solar cells may be improved from a theoretical point of view.

Crystal structures

Perovskites, with formula ABX_3, typically have unit cells composed of five atoms in a cubic structure (α phase), where cation B has six nearest neighbor anions X and cation A has twelve (Fig. 1(a)). Under ideal conditions, to maintain high-symmetry cubic structure, the ionic radii of A, B, and X should satisfy the requirement that the tolerance factor t ($t = (R_A + R_X)/\{\sqrt{2}(R_B + R_X)\}$) should be close to 1, where R_A, R_B, and R_X are the ionic radii of the corresponding ions. Otherwise, the cubic structure will be distorted and crystal symmetry is lowered. Of note, to satisfy $t \approx 1$, the A ion must be much larger than the B ion. In halide perovskites, the B site is usually occupied by a large Pb or Sn atom, so A must be extremely large. Cs is almost the largest group-I element in the periodic table. However, Cs is still not large enough to hold the stable cubic perovskite structure, so it must be replaced with a larger molecule. This may be a reason that $CH_3NH_3PbI_3$ is more stable and performs better than $CsPbI_3$.

At finite temperature, a cubic structure may exist when t lies between 0.89 and 1.[73] Generally, smaller t could lead to lower-symmetry tetragonal (β phase) or orthorhombic (γ phase) structures, whereas larger t ($t > 1$) could destabilize the three-dimensional (3D) B–X network, leading to a two-dimensional (2D) layer structure. Notably, in DFT calculations at zero temperature, the γ phase is always the most stable, and the α phase is always the most unstable, because it is difficult to satisfy $t = 1$. However, transitions between those structures at finite temperature often occur in most perovskites.[74,75] In fact, the soft transverse acoustic phonon mode makes the anion X easily displaced from the B–B midpoint of the ideal cubic phase. At finite temperature, such displacements are likely to be dynamic in nature.[74] Due to different ion sizes and structural stabilities, the transition temperatures of different perovskites vary. For the archetypal halide perovskite $CH_3NH_3PbI_3$, the α to β to γ phase transitions occur at 330 K and 160 K, respectively.[76] Interestingly, a non-perovskite δ phase was found for perovskites such as $HC(NH_2)_2PbI_3$, $FAPbI_3$, $CsPbI_3$ and $CsSnI_3$.[74,75,77]

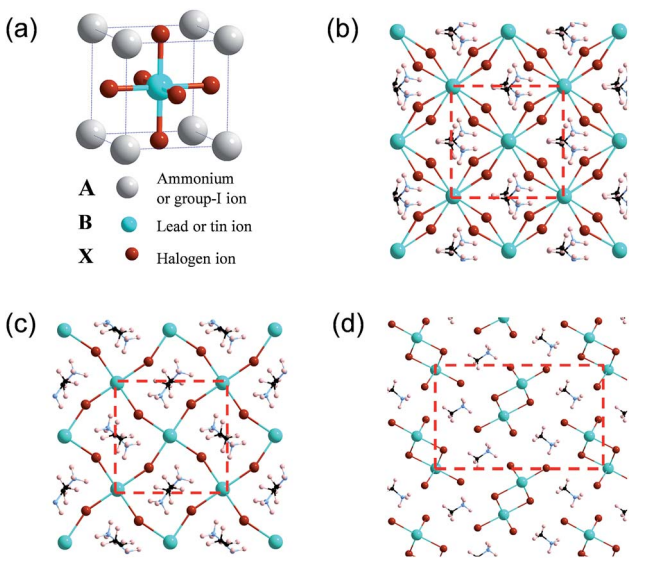

Fig. 1 The atomic structure of (a) α phase, (b) β phase, (c) γ phase, and (d) δ phase $CH_3NH_3PbI_3$. The unit cells of β and γ phases are ($\sqrt{2} \times \sqrt{2} \times 2$), based on the α phase. Reprinted with permission from ref. 62.

 This journal is © The Royal Society of Chemistry 2015

Published on 21 October 2014. Downloaded by ENEA - CASSACCIA on 12/06/2016 17:53:20.

Unlike β and γ phases, the δ phase cannot be derived from the α phase by B–X–B bond angle distortion. Instead, the B–X bond is broken (see Fig. 1(d)).

The atomic structures of organic–inorganic perovskites are more complicated than those of inorganic perovskites, because noncentrosymmetric organic molecules have many possible orientations. For $CH_3NH_3PbI_3$, the CH_3NH_3 molecules in the high-temperature α phase are randomly orientated and the overall crystals preserve O_h symmetry. In the medium temperature β phase, the freedom of CH_3NH_3 molecules is somewhat reduced but their orientations are still disordered. In the low-temperature γ phase, the CH_3NH_3 molecules are frozen and have fixed alignments.[74]

The disorder of the molecules' orientations in α and β phases is impossible to simulate in a finite unit cell. For the α phase, we compared the total energies of $CH_3NH_3PbI_3$ with the C–N bond along [001], [110], and [111] directions and found that the system is the most stable with a C–N bond along the [111] direction. The physical properties of the α phase were calculated with the C–N bond along the [111] direction and the β phase is constructed accordingly. We note that other calculations show that [001] is the most stable direction, although their difference is very small. Also, the basic electronic structure of $CH_3NH_3PbI_3$ does not sensitively dependent on the direction of CH_3NH_3 molecules.

The calculated and experimental lattice parameters of α, β, γ and δ phases are shown in Table 2. We can see that generally LDA underestimates lattice parameters and GGA overestimates lattice parameters. This finding is consistent with the results for conventional semiconductors. However, for $CH_3NH_3PbI_3$, the overestimation of GGA(PBE)-calculated lattice parameters was attributed to the neglect of van der Waals interactions between the CH_3NH_3 and [Pb–I] frameworks.[71] When dispersive interactions with particular form are considered, the calculated lattice parameters match experimental results well.[46,47,71] Based on this, the van der Waals interaction was claimed to be an important factor in hybrid halide perovskites.[71] However, we posit that the importance of van der Waals interactions should be carefully revisited for two reasons. One, GGA/PBE overestimates lattice parameters not only for $CH_3NH_3PbI_3$ but also for other compounds, as this is an intrinsic problem of exchange–correlation functional not of particular material. Two, for inorganic $CsPbI_3$, when the dispersive interaction is included, the calculated lattice parameters can also be in agreement with experimental ones.[46] Therefore, it could be that the GGA underbinds the compound. Adding dispersive interactions increases the binding of the compound and corrects GGA errors. It does not necessarily mean that the dispersive interaction is intrinsic to halide perovskites. Corrections can also be achieved by mixing LDA and GGA, since LDA generally overbinds compounds. Following this reasoning, CH_3NH_3 behaves like an ion, and the interaction between CH_3NH_3 and [Pb–I] is similar to that between Cs and [Pb–I], which exhibits ionic character.

Table 2 The calculated lattice constants and band gaps of the three phases of $CH_3NH_3PbX_3$ (X = I, Br, Cl) are compared with the experimental ones. Because the CH_3NH_3 molecule is noncentrosymmetric, for the α phase, the calculated pseudocubic lattice constant is defined by $a = V^{1/3}$ and for the β phase, $a = \frac{1}{2}(a + b)$. The relative total energy (meV per formula unit), referred to the α phase, is also given. For HSE + SOC, 43% portion of exact-exchange is chosen to reproduce the band gap of the β phase $CH_3NH_3PbI_3$ as in ref. 81. Reprinted with permission from ref. 70

		Lattice constant (Å)		Relative energy (meV)			Band gap (eV)			
Phase	Symmetry	PBE	Exp	PBE	PBE + SOC	HSE + SOC	PBE	PBE + SOC	HSE + SOC	Exp
$CH_3NH_3PbI_3$										
α	$Pm\bar{3}m$	$a = 6.39$	$a = 6.31$,[75] 6.28 (ref. 74)	0	0	0	1.53	0.46	1.14	
β	$I4/mcm$	$a = 8.80$, $c = 12.99$	$a = 8.85$,[74,75] 8.88,[116] $c = 12.64$,[75] 12.67 (ref. 116)	−93	−127	−100	1.57	0.77	1.60	1.52,[75] 1.5 (ref. 17)
γ	$Pbnm$	$a = 8.84$, $b = 8.77$, $c = 12.97$	$a = 8.84$,[74] $b = 8.56$,[74] $c = 12.58$,[74]	−38	−55	−50	1.46	0.59	1.43	
$CH_3NH_3PbBr_3$										
α	$Pm\bar{3}m$	$a = 6.04$	$a = 5.94$,[34] $a = 5.95$ (ref. 132)	0	0	0	1.93	0.89	1.92	2.23,[117] 2.32,[127] 2.29,[34,125] 2.35 (ref. 132)
β	$I4/mcm$	$a = 8.28$, $c = 12.25$		−60	−59	−92	1.98	1.13	2.11	
γ	$Pbnm$	$a = 8.32$, $b = 8.29$, $c = 12.15$		−21	−19	−44	1.81	0.91	1.86	
$CH_3NH_3PbCl_3$										
α	$Pm\bar{3}m$	$a = 5.78$	$a = 5.70$ (ref. 129)	0	0	0	2.40	1.33	2.57	3.11 (ref. 132)
β	$I4/mcm$	$a = 7.93$, $c = 11.71$		−52	−53	−65	2.47	1.57	2.77	
γ	$Pbnm$	$a = 7.94$, $b = 7.95$, $c = 11.66$		−12	−16	−18	2.27	1.31	2.47	

Published on 21 October 2014. Downloaded by ENEA - CASSACCIA on 12/06/2016 17:53:20.

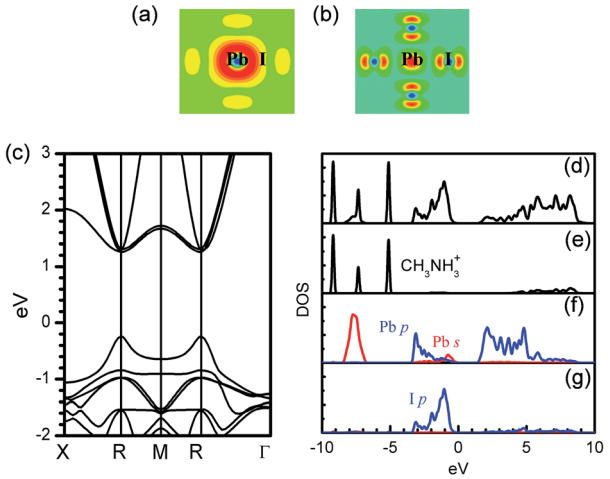

Fig. 2 The (a) partial charge density of the CBM, (b) partial charge density of the VBM, (c) band structure, and (d) DOS of $CH_3NH_3PbI_3$ using DFT–PBE calculations. Modified with permission from ref. 63.

Electronic structures

We calculated the band structure, (partial) density of states (DOS) and partial charge density of valence band maximum (VBM) and conduction band minimum (CBM) states of α phase $CH_3NH_3PbI_3$ using DFT–PBE (Fig. 2). The direct bandgap is at the *R* point. Unlike most cations whose outer s orbitals are empty, Pb has an occupied 6s orbital, which is below the top of valence bands of perovskites. This so-called lone pair of s electrons in Pb often gives rise to unusual properties.[78–80] DOS and partial charge density plots show that the VBM has strong Pb s and I p antibonding character, whereas the CBM is almost contributed from the Pb p state, which reflects the unique dual nature (ionic and covalent) of halide perovskites' electronic structures. In conventional semiconductors such as GaAs and CdTe, the CBM primarily has s orbital character, whereas the VBM primarily has p orbital character. In contrast, halide perovskites exhibit inverted band structure. The state contributed by the organic molecule is far from the band edges, which means that the organic molecule does not play a direct role in determining the basic electronic structures in halide perovskites. As discussed above, an important role of organic molecules in halide perovskites is stabilizing the perovskite structure and changing the lattice constant. Other possible effects of organic molecules, such as dipole polarization, are discussed later.

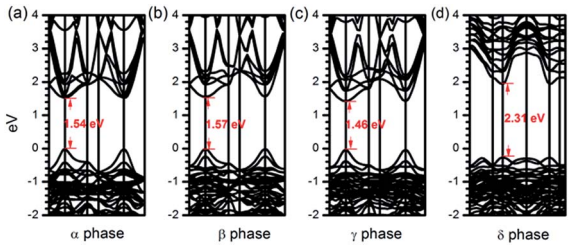

Fig. 3 Band structure of (a) α phase, (b) β phase, (c) γ phase, and (d) δ phase $CH_3NH_3PbI_3$. The α phase is calculated using the same tetragonal supercell as for β and γ phases. Reprinted with permission from ref. 62.

The band structures of β, γ, and δ phase $CH_3NH_3PbI_3$ are shown in Fig. 3. The band structure of the α phase with a $(\sqrt{2} \times \sqrt{2} \times 2)$ supercell is also shown for comparison. These calculations suggest that β and γ phases have band structures similar to the α phase, which indicates that the Pb–I–Pb bond angle distortions do not significantly change the electronic structures. However, the band structure of the δ phase is distinctive. The partial Pb–I bonds are broken and the 3D [Pb–I] framework is destroyed in the δ phase. In this phase, the coupling between Pb s and I p is weakened. As a result, the VBM, which is the s–p antibonding state, drops in energy, leading to an enlarged bandgap and a flat upper valence band. In experiments, the δ phase is usually yellow and has a bandgap of over 2 eV,[74,75] *i.e.*, more than 0.5 eV larger than that of the other phases. Its hole effective mass is expected to be much larger than that of other perovskite phases.

The DFT–PBE calculated bandgap for β phase $CH_3NH_3PbI_3$ is 1.57 eV, which is in good agreement with experiments. However, this result is a fortuitous one, due to the accidental canceling-out of underestimating GGA and neglecting SOC.[66] This is not observed in other perovskites such as $CH_3NH_3PbBr_3$, $CH_3NH_3PbCl_3$ and $CsPbI_3$, whose GGA-calculated bandgaps are lower than experimental values. In those cases, advanced computational methods such as PBE + SOC,[66,68] HSE + SOC,[81] and GW + SOC[57,59,60] have been used to study the electronic structure of $CH_3NH_3PbI_3$ and other perovskites. Notably, the key features of GGA-derived electronic structures, such as strong sp coupling and dual nature of bond characters, do not change with advanced methods. In fact, the SOC effect is not a unique finding for $CH_3NH_3PbI_3$. Heavy atoms such as Pb and Bi have large SOC effects, which also exists in semiconductors like PbTe[80] and Bi_2Se_3.[82] For those compounds, even though the band degeneracy and symmetry will change when the SOC effect is included in calculations, the electronic structures and band character can be well described by non-SOC calculations.

Pb chalcogenides exhibit abnormal bandgap changes with lattice constant and strain.[80] Lang *et al.*[68] demonstrated that the bandgap increases from $CsPbI_3$, to $CH_3NH_3PbI_3$, to $FAPbI_3$. This is expected since the VBM has strong antibonding character and will drop when the lattice constant increases. However, the experimental bandgaps of $CsPbI_3$ (1.67 eV), $CH_3NH_3PbI_3$ (1.52 eV), and $FAPbI_3$ (1.48 eV) do not follow the theoretical trends. Furthermore, the trend is even more ambiguous when considering bandgaps of $CsSnI_3$ (1.30 eV), $CH_3NH_3SnI_3$ (1.20 eV) and $FASnI_3$ (1.41 eV). Bandgaps' relations to the lattice constant and crystal structures should be carefully revisited both in experiment and theory to address these uncertainties.

Ambipolar conductivity

The effective mass (m^*) of electrons (holes) around the bottom of the conduction band (top of the valence band) can be

 This journal is © The Royal Society of Chemistry 2015

Published on 21 October 2014. Downloaded by ENEA - CASSACCIA on 12/06/2016 17:53:20.

approximately fitted by $m^* = \hbar^2 \left[\frac{\partial^2 \varepsilon(k)}{\partial^2 k}\right]^{-1}$, where $\varepsilon(k)$ are energy dispersion relation functions, which are typically described by band structures. Intuitively, the more dispersive (flat) the band near the band edges is, the lighter (heavier) the effective mass is. In conventional thin-film solar cell absorbers, such as GaAs and CdTe, the CBM is mostly contributed by cation s and anion s orbitals, and the VBM is mostly contributed by\ anions' p character (p–s semiconductor). High-energy-level s orbitals are more delocalized than low-energy-level p orbitals and thus the lowest conduction band is more dispersive than the highest valence band. Consequently, the electron effective mass is much smaller than the hole effective mass. That is why electrons transport much faster than holes, and why the second-generation thin-film solar cell must use p-type absorbers.

The existence of lone-pair Pb s electrons makes the situation dramatically different in perovskite solar cells. The electronic structure of $CH_3NH_3PbI_3$ is inverted compared to conventional p–s semiconductors. Its CBM is derived from Pb p orbitals, and the VBM is a mixture of Pb s and I p (s–p semiconductor) orbitals. Even though the CBM comes from p orbitals, a cation Pb p orbital has a much higher energy level than anion p orbitals, as in p–s semiconductors. Therefore, the lower conduction band of $CH_3NH_3PbI_3$ is more dispersive than the upper valence band in p–s semiconductors. On the other hand, due to strong s–p coupling around the VBM, the upper valence band of $CH_3NH_3PbI_3$ is dispersive. The DFT–PBE calculated electron and hole effective masses of α phase $CH_3NH_3PbI_3$, together with typical first and second-generation solar cell absorbers, are listed in Table 3. We can find that the hole effective mass of $CH_3NH_3PbI_3$ is balanced with the electron effective mass. The balanced effective mass in $CH_3NH_3PbI_3$ may lead to ambipolar conductivity[65] in perovskite solar cells, which facilitates the p–i–n junction solar cell. It is noted that the effective mass calculated by the GW + SOC method[57] is even lower, indicating that the many-body effect may play a role for small carrier effective mass.

High optical absorption

One of the superior performance aspects of perovskite solar cells is high optical absorption, such that the absorber layer, which is less than 500 nm thick, can absorb enough sunlight to achieve high efficiency above 15%. The photoactive layer is even thinner since the mesoscopic absorber layer includes additional scaffold oxides (TiO_2, ZrO_2, or Al_2O_3). In comparison, the thicknesses of the absorber layers in first- and second-generation solar cells are about 300 μm and 2 μm, respectively.

First-principles calculations have been used to calculate the optical absorption of halide perovskites and to unravel the physics underlying this property. The optical absorption of a semiconductor is fundamentally determined by two factors. One is the transition matrix elements between valence band (VB) states and conduction band (CB) states, and the other is their joint density of states (JDOS). The former measures the probability of each photoelectric transition, and the latter measures the total number of possible photoelectric transitions. Thus, the optical absorption coefficient of a material is closely related to its electronic structure.

The mechanisms of optical absorption for first-generation, second-generation, and perovskite-based solar cell absorbers are depicted schematically in Fig. 4. For the first-generation absorber (silicon), the optical absorption close to the band edge is from the Si p orbital to the Si p and s orbitals. However, silicon is an indirect bandgap semiconductor and its transition probability between band edges is two orders of magnitude lower than that of the direct bandgap, making its absorber layer two orders of magnitude thicker and increasing the cost of

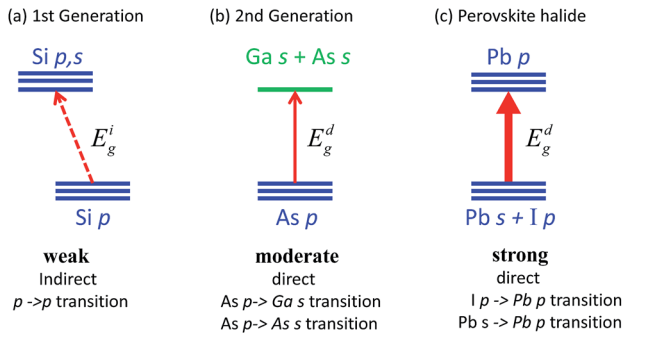

Fig. 4 The schematic optical absorption of (a) first-generation, (b) second-generation, and (c) halide perovskite solar cell absorber. GaAs has been chosen as a prototypical second-generation solar cell absorber.

Table 3 DFT–PBE calculated effective masses for electrons and holes

	Electron effective mass (m_e)	Hole effective mass (m_e)
$CH_3NH_3PbI_3$	0.35, 0.32 (ref. 65)	0.31, 0.36 (ref. 65)
$CH_3NH_3PbI_3$ (SOC)	0.18, 0.23 (ref. 65)	0.21, 0.29 (ref. 65)
$CsSnI_3$	0.19	0.09
$CsSnI_3$ (SOC)	0.16	0.07
Silicon	0.26	0.29
GaAs	0.07	0.34
$CuInSe_2$	0.09	0.75
$Cu_2ZnSnSe_4$	0.10	0.26
CdTe	0.09	0.28

Published on 21 October 2014. Downloaded by ENEA - CASSACCIA on 12/06/2016 17:53:20.

materials. The bandgaps of the second-generation absorber (GaAs as an example) and halide perovskite ($CH_3NH_3PbI_3$ as an example) are direct and thus their optical absorption is much stronger than that of silicon. However, the electronic structures of GaAs and $CH_3NH_3PbI_3$ are different. The lower part of the GaAs CB is derived from the dispersive s band (delocalized s orbitals), whereas the lower part of the $CH_3NH_3PbI_3$ CB is mainly composed of degenerate Pb p bands. The atomic p orbital exhibits less dispersion than s orbitals do. As a result, the DOS in the lower CB of the halide perovskites is significantly higher than that of GaAs as shown in Fig. 5(a), leading to a higher JDOS (Fig. 5(b)). Additionally, the edge transition for $CH_3NH_3PbI_3$ comes from mixed-(Pb s, I p) to Pb p orbitals. The intra-atomic Pb s to Pb p transition probability is high, which makes the VBM–CBM transition probability of $CH_3NH_3PbI_3$ comparable to that of GaAs. Therefore, halide perovskites show stronger optical absorption than GaAs. The calculated optical absorption coefficients of $CH_3NH_3PbI_3$ and GaAs are shown in Fig. 5(c). It is seen that the optical absorption coefficient of $CH_3NH_3PbI_3$ is up to 1 order of magnitude higher than that of GaAs within the visible light range. Because visible light accounts for the major usable portion of the full solar spectrum, high absorption in its range is critical for achieving high-efficiency cells.

Achieving high optical absorption is crucial for realizing economic and efficient solar cells with extremely thin absorbers. However, the effect of the optical absorption coefficient is not considered in the well-known Shockley–Queisser limit.[43] In a real-world solar cell, the theoretical maximum efficiency depends on the thickness of the absorber layer. Recently, Yu *et al.*[83,84] took the absorption coefficient and absorber layer thickness into consideration and developed a method to calculate the maximum efficiency based on the absorber thickness. Using this approach, we have calculated the

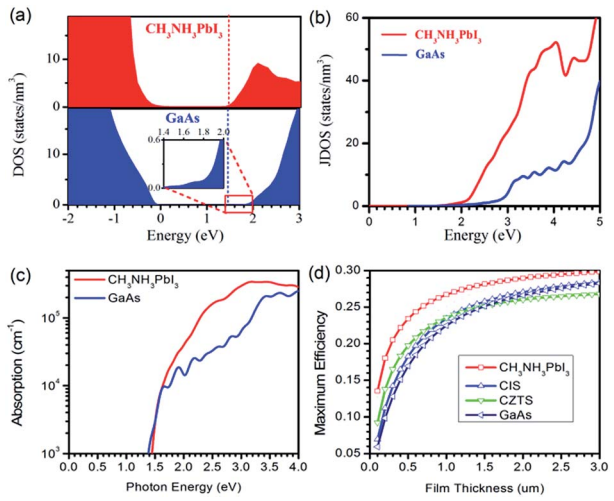

Fig. 5 (a) Electronic density of states (DOS) of $CH_3NH_3PbI_3$ and GaAs. The VBMs are referred to as zero energy and CBMs are marked as dashed lines. (b) The JDOS of $CH_3NH_3PbI_3$ and GaAs. (c) The optical absorptions of $CH_3NH_3PbI_3$ and GaAs. (d) Calculated maximum efficiencies of $CH_3NH_3PbI_3$, $CuInSe_2$(CIS), Cu_2ZnSnS_4(CZTS), and GaAs as a function of film thickness. Modified with permission from ref. 62.

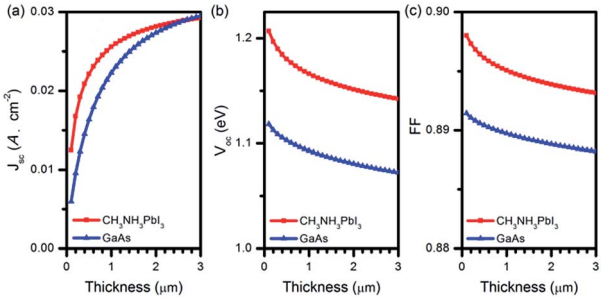

Fig. 6 The calculated ideal device performances of (a) J_{sc}, (b) V_{oc}, and (c) FF for $CH_3NH_3PbI_3$- and GaAs-based thin-film solar cells as a function of thickness.

maximum efficiencies of perovskites and other mainstream thin-film absorbers. The results are shown in Fig. 5(d).[62] The halide perovskites ($CH_3NH_3PbI_3$ and $CsPbI_3$) exhibit much higher conversion efficiencies than GaAs, CIS, and CZTSe for any given thickness. More importantly, the halide perovskites are capable of achieving high efficiencies with very thin absorber layers. For example, with a 0.3 μm absorber (similar to the thickness of $CH_3NH_3PbI_{3-x}Cl_x$ in the 15.4% perovskite-based cell[7]), $CH_3NH_3PbI_3$-based cells have a maximum efficiency of 21%, while it is only 13% for a GaAs-based solar cell. The results are consistent with many of today's most common thin-film solar cells (GaAs, CdTe, CIGS, and CZTSS) – the absorbers must be about 2 μm thick to achieve high efficiencies.[85]

Following the idea of Yu *et al.*,[83,84] we have also developed methods to calculate the thickness-dependent maximum solar cell parameters of $CH_3NH_3PbI_3$. Parameters such as short-circuit current (J_{sc}), open-circuit voltage (V_{oc}), and fill factor (FF) as a function of absorber thickness for $CH_3NH_3PbI_3$ and GaAs based thin-film solar cells are shown in Fig. 6. The experimentally achieved J_{sc} (21.5 mA cm^{-2}) and V_{oc} (1.07 eV) in $CH_3NH_3PbI_3$-based solar cells with a film thickness of 0.33 μm (ref. 7) are very close to our calculated theoretical limits for J_{sc} (19.2 mA cm^{-2}) and V_{oc} (1.19 eV) at 0.30 μm. The bottleneck for present $CH_3NH_3PbI_3$-based solar cells is the relatively low FF (67%), which should be limited by the non-ideal band offsets between the perovskite absorber layer and the interfaces at the contact layer. Our results demonstrate that thin-film solar cells based on the $CH_3NH_3PbI_3$ perovskite have the capability to achieve a high FF. Improved interfaces and contact layers in solar cells should significantly improve the cell performance, which is consistent with recent work on interface engineering and uniform growth to avoid the shunting resistance.

Superior point defect properties

In first- and second-generation solar cells, defect and doping properties were crucial factors affecting the cell performance. The key component was the p–n junction, where the photogenerated electrons and holes are separated and collected with the aid of the internal electric field. The p or n-type absorbers were made from materials with intrinsic defects, or using

 This journal is © The Royal Society of Chemistry 2015

Published on 21 October 2014. Downloaded by ENEA - CASSACCIA on 12/06/2016 17:53:20.

intentional doping. On the other hand, intrinsic defects that create deep energy levels in the absorber usually act as Shockley–Read–Hall nonradiative recombination centers and carrier traps, reducing the carrier lifetime and thus V_{oc}. A good solar cell absorber must exhibit proper doping and defect properties. For example, the V_{oc} of a next-generation solar cell absorber, $Cu_2ZnSn(S,Se)_2$, is much lower than its bandgap, and its record efficiency is about 12%.[85] This could be related to the energetically favorable formation of the dominating defect in $Cu_2ZnSnSe_2$, Cu_{Zn}, which can pin the n-type Fermi energy. It may also be due to the formation of a Sn_{Zn} deep level, which may become a carrier trap and nonradiative recombination center.[86,87]

It is still under debate whether a perovskite solar cell functions more like a dye-sensitized solar cell or thin-film solar cell. In a dye-sensitized solar cell, TiO_2 acts as an electron acceptor to aid electron transport. However, experiments by Snaith's group demonstrated that perovskites can transport electrons by itself, without scaffold TiO_2.[7,9] Subsequent characterizations found both positive[88] and negative[89] effects of TiO_2 for solar cell function. Although the underlying mechanism of perovskites is unclear, point defects inevitably exist due to low-temperature solution based processes, making perovskites unintentionally doped. Interestingly, Laban and Etgar[90,91] found p-type $CH_3NH_3PbI_3$ while You *et al.*[92] found n-type, meaning that $CH_3NH_3PbI_3$ is bipolarly dopable and different processes can lead to opposite doping behaviors.

Several types of defects, including both donor-like and acceptor-like, exist in semiconductors. The relative concentrations of those donors and acceptors, which are directly related to the defect formation energies, determine p or n-type conductivity. The formation energy of a defect depends on the chemical potential μ, which corresponds to environmental factors such as precursors, partial pressure and temperature. In this way, the experimental conditions determine the formation energies of all the possible defects and thus impact the polar conductivity in the product material.

First-principles calculations have been used to study the point defect properties of α phase $CH_3NH_3PbI_3$.[63] The chemical potentials for equilibrium-growth are as shown in Fig. 7(a), which indicates that growth of $CH_3NH_3PbI_3$ can occur only in a long and narrow range of chemical potential. Otherwise, secondary phases, such as PbI_2 and CH_3NH_3I, would also form. Three typical chemical potentials (A, B, and C in Fig. 7(a)) were chosen to study the formation energies of point defects. All the possible point defects, including three vacancies (V_{MA}, V_{Pb}, V_I), three interstitials (MA_i, Pb_i, I_i), two cation substitutions (MA_{Pb}, Pb_{MA}) and four antisite substitutions (MA_I, Pb_I, I_{MA}, I_{Pb}), were considered in our calculations. The formation energies of these point defects as a function of Fermi level position at chemical potentials A, B, and C are shown in Fig. 7(b)–(d) respectively. The lowest crossing points between donor and acceptor indicate the positions of Fermi level pinning. The conductivity of $CH_3NH_3PbI_3$ can arise from intrinsically good p-type conduction, but interestingly, it can also arise from moderate to good n-type conduction when the chemical potential is at A (I-rich/Pb-poor), B (moderate), or C (I-poor/Pb-rich). Such flexible defect

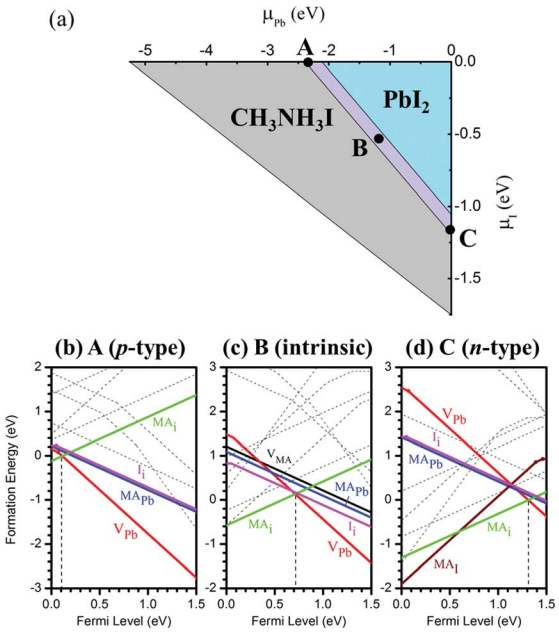

Fig. 7 The achievable chemical potentials for thermo-equilibrium growth of $CH_3NH_3PbI_3$ and the formation energies of intrinsic point defects in $CH_3NH_3PbI_3$ at chemical potentials A, B, and C. Defects with much higher formation energies are displayed as dashed lines. Modified with permission from ref. 63.

properties are distinct from those of conventional thin-film solar cell absorber CIGS[93] and CZTSS.[94] This is due to the chemical similarity of the cations and the presence of Cu antibonding d orbitals at the VBM, which means that acceptors such as V_{Cu}, Cu_{Ga}, and Cu_{Zn} have very low formation energies. Thus, in equilibrium growth, p-type doping in CIGS and CZTSS is easy but n-type doping is difficult due to self-compensation.[93] In $CH_3NH_3PbI_3$, the dominant donor MA_i and dominant acceptor V_{Pb} have comparable formation energies, so both p-type and n-type doping are possible in $CH_3NH_3PbI_3$. Our theoretical results on bipolar conductivities are consistent with the experimental findings of both p and n-type $CH_3NH_3PbI_3$ in different growth processes.

Defect formation energies determine the polar conductivity of a semiconductor, whereas defect transition levels determine the electrical effect of any particular defect. The transition level of a defect is the Fermi level position where the defect can gain or lose electrons and change its charge state. Shallow defect levels, close to band edges, can donate or accept electrons to bulk bands and become effective doping methods for absorbers. However, deep level defects, near the middle of the bandgap, can trap electrons or holes and become SRH nonradiative recombination centers in the absorber. The transition levels of all possible point defects in $CH_3NH_3PbI_3$ are shown in Fig. 8. The defects with low formation energies, as shown by the solid lines in Fig. 7(b)–(d), have transition energies less than 0.05 eV above (below) VBM (CBM). All defects that create deep levels have high formation energies, as shown by the dashed lines in Fig. 7(b)–(d). Besides point defects, Kim *et al.*[64] used DFT–GGA to calculate the DOS and partial charge densities of

Published on 21 October 2014. Downloaded by ENEA - CASSACCIA on 12/06/2016 17:53:20.

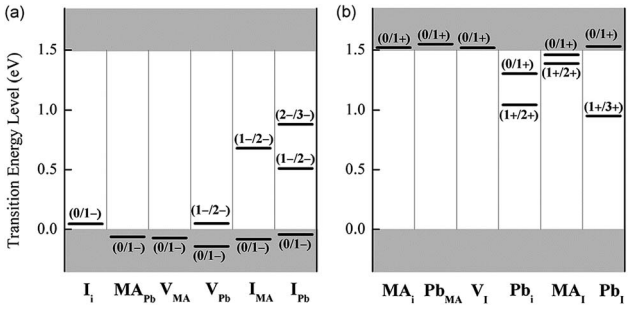

Fig. 8 The transition energy levels of (a) intrinsic acceptors and (b) intrinsic donors in $CH_3NH_3PbI_3$. Zero in energy is referred to the VBM. Reprinted with permission from ref. 63.

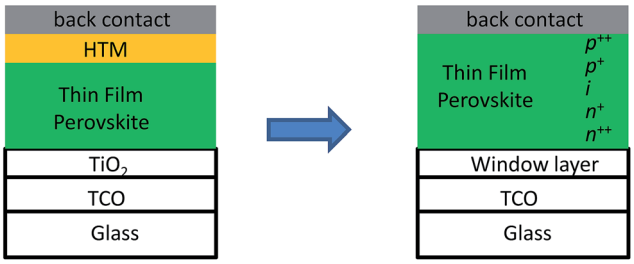

Fig. 9 The proposed hole-conductor-free perovskite solar cell without HTM layer by utilizing p-type doping.

two types of neutral defects in β phase $CH_3NH_3PbI_3$: Schottky defects (equal numbers of positive and negative vacancies) and Frenkel defects (equal numbers of vacancies and interstitials of the same ion). They found that those defect pairs do not create deep gap states. Du[81] used DFT–PBE calculations and similarly found that in β phase $CH_3NH_3PbI_3$, most of the point defects are shallow. Alternatively, he found that for the I interstitial, a particular configuration may be a deep state, with a role in electrical properties. So far, it is not clear whether the deep I interstitial state in Du's calculation is derived from different crystal phases or particular defect structures.

Shallow defect properties are closely related to the dual-nature electronic structures of halide perovskites. The shallow dominant acceptors V_{Pb} and MA_{Pb} originate from covalent coupling between the Pb lone-pair s and I p orbitals, which increases the VBM so that the acceptors are generally shallower than in cases without strong sp coupling. The mechanism is similar for the shallow V_{Cu} in CIGS, where the VBM is increased by coupling between the Cu d and Se p orbitals.[93] The shallow donors MA_i and V_I are due to the high ionicity. The MA_i has no covalent bonds to the Pb–I framework and does not create additional gap states. For V_I, our previous study has shown that weak covalence generally leads to the shallow anion vacancy levels.[95]

The tunable polar conductivity and shallow defect properties may help explain why high-performance perovskite solar cells, with extremely long carrier lifetimes,[96,97] can be produced by a diverse range of growth approaches and a wide variety of solar cell architectures. The superior point defect properties would suggest new architectures for perovskite solar cell architecture. The two prevailing architectures are mesoscopic and planar structures. The former mostly use porous TiO_2 to help electron transport while the latter do not. Both need a hole transport material (HTM) layer to support hole transportation from the perovskite absorber to contact. Organic HTMs are expensive and many researchers are seeking inorganic materials as economic substitutes,[98–100] even though they generally do not behave as well as organic ones. However, the HTM layers are not necessary if the absorber can be effectively p-type doped as proposed in our theory above. In this case, the HTM layer would be replaced by the p-type perovskite layers. Electrons and holes can be separated through an intrinsic p–i–n junction, as depicted in Fig. 9. Recently, several reports[91,101–103] have been published on the effective performance of hole-conductor-free perovskite solar cells, demonstrating the potential applications of p–i–n homojunctions in solar cells. Alternatively, Agiorgousis *et al.*[104] found that deep point defect levels could exist through large atomic relaxations which they attributed to the strong covalency of the system.

Electrically benign structural disorder

Most of the current theoretical studies on halide perovskites are based on ordered structures such as α, β, and γ phases. However, perovskite structures in real devices have been found to be disordered and complicated.[105] In a mesoscopic-structure solar cell, the optically active perovskites are integrated into a mesoporous network of TiO_2 or Al_2O_3, where the majority of the layers is optically inert scaffold oxide. Experimentally, it is difficult to determine the structure of minor perovskite embedded within the oxides' irregular pores using conventional crystallographic methods. Recently, Choi *et al.*[105] reported the first fully quantitative structural characterization of $CH_3NH_3PbI_3$ within mesoporous TiO_2 using atomic pair distribution analysis of high energy X-ray diffraction. They found that most of $CH_3NH_3PbI_3$ (70%) is highly disordered with local perovskite structure extending over a range of only 1.4 nm, which is about 2 lattice constants of the α phase. The mesoporous scaffold confined the perovskite within the pores and reshaped the structures of perovskites. On the other hand, the low-temperature growth process inevitably leads to polycrystalline perovskites with grain boundaries (GBs). Currently, there are no experimental investigations on the structural and electronic properties of those structural disorders and topological defects, because high-quality material is required for high resolution transmission spectroscopy (HRTEM), and the organic molecule in halide perovskites could be easily broken under a high-energy electron beam. Alternatively, theoretical calculations[69] can provide direct insights into the electrical properties of structural disorders and topological defects in hybrid perovskites.

In conventional polycrystalline light absorbers, GBs could dramatically alter the electronic and optical properties from those of the single-crystal phase. GBs are usually detrimental to solar cell performance. For example, our recent first-principles calculations showed that many intrinsic GBs in solar cell

 This journal is © The Royal Society of Chemistry 2015

Published on 21 October 2014. Downloaded by ENEA - CASSACCIA on 12/06/2016 17:53:20.

absorbers CdTe,[106,107] $CuInSe_2$,[108] and $Cu_2ZnSnSe_2$ (ref. 109) create deep defect levels in the bandgaps, acting as carrier traps and nonradiative recombination centers that harm carrier lifetime and device performance in solar cells. We further found that the detrimental intrinsic GB behaviors in thin-film solar cell absorbers originated from the formation of undesirable chemical bonds, especially anion–anion bonds at the structural core of GBs. To reduce these detrimental activities, specific post-processing treatments are required for polycrystalline silicon, CdTe, and CIGS cells. For example, Cl-treatment in experiments enhanced the efficiency of CdTe solar cells. Recent combined theoretical and experimental studies[106] have demonstrated that Cl segregated into the GB part of polycrystalline CdTe solar cells, effectively taming the detrimental effects at GBs. In addition, unintentional passivation at GBs by defect segregations has been shown to be important in high-efficiency CIGS[108] and CZTS[109] solar cells. Therefore, solar cells based on polycrystalline thin-film semiconductors often require intentional or unintentional passivation to achieve improved carrier lifetime and V_{oc}. Interestingly, high-efficiency perovskite solar cells may not require such treatment. Edri *et al.*[110] measured the electron beam induced current (EBIC) on as-grown $CH_3NH_3PbI_3$ and found that the EBIC contract from the GBs of the polycrystalline $CH_3NH_3PbI_3$ sample is not different from that of grains themselves, indicating negligible charge separation and recombination occurred at GBs. According to their results, GBs in $CH_3NH_3PbI_3$ are almost electrically invisible. It is unclear whether such benign GB properties are intrinsic, or arise from other effects such as unintentional defect segregations. We therefore investigated what causes such different GB properties in perovskites *versus* conventional thin-film absorbers.

We used first-principles calculations to investigate the electronic properties of GBs in halide perovskites. We chose two types of GBs as indicated in Fig. 10 as model systems, because those structures are low-energy and have been observed in large abundance in $SrTiO_3$, a model perovskite oxide. Both are rich in disordered configurations such as distorted bond angles, I–I wrong bonds, Pb dangling bonds, and I dangling bonds. Thus they represent the general features of GBs in polycrystalline perovskites.

Due to the structural complicity of $CH_3NH_3PbI_3$, the GB structures were constructed based on $CsPbI_3$. The DOS of those GBs are shown in Fig. 10(a)–(i) and compared to that of single-crystal phase $CsPbI_3$. We can see that the DOS of the supercells with GBs are very similar to those of single-crystal phases. None of these GBs introduce defect states within the bandgap region. The results, therefore, suggest that GBs in halide perovskites are electrically benign. Such intrinsically clean GB behaviors have not been seen in other solar cell absorbers such as CdTe,[107] $CuInSe_2$,[108] and $Cu_2ZnSnSe_4$.[109]

The electrically benign nature of GBs in halide perovskites is closely related to their electronic structures. The origin of the deep gap state in CdTe GBs, with comparisons to halide perovskites, is shown in Fig. 11. Te–Te wrong bonds at the GBs in CdTe introduce deep defect levels, which are the antibonding ppσ* states of the Te–Te bond. Similarly, in the perovskites, the I–I wrong bonds also create antibonding ppσ* states in the Σ5(311) GB. However, the ppσ* state is not as deep as in CdTe. There are two reasons for this. First, the VBM in halide perovskites is much higher than I 5p, because strong Pb 6s and I 5p coupling significantly increases the VBM level. Higher VBM means shallower defect levels. Second, the I–I interaction in halide perovskites is weaker than the anion–anion interaction in chalcogenides due to the larger distances for the I–I pair. As evidence, the Se–Se bond length in the CZTSe Σ3(114) GB is 2.50 Å,[109] which is much shorter than the I–I bond length (3.70 Å) at the Σ5(310) GB in $CsPbI_3$. Also, the Se–Se bond length is 1.11 times of the ionic size of Se^{2-}, whereas the I–I bond length is 1.48 times of ionic size of I^{1-}.

The large I–I bond length in halide perovskites is a consequence of its extremely large lattice constant due to the previously mentioned large A and B atoms in halide perovskites. As discussed, A should be larger than B due to the structural stability requirement. In Pb-based perovskites, the Pb atom at the B site is large, and the Cs atom or CH_3NH_3 molecule at the A

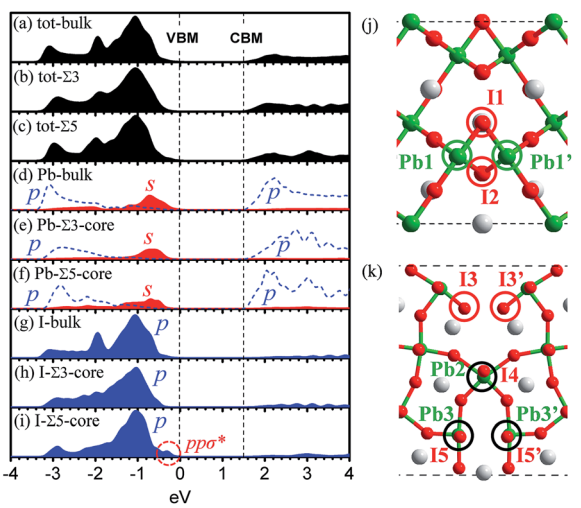

Fig. 10 (a–i) are (partial) DOS of pristine $CsPbI_3$ and polycrystalline $CsPbI_3$ with Σ3(111) and Σ5(310) GBs. (j) and (k) are atomic structures at Σ3(111) and Σ5(310) GBs respectively.

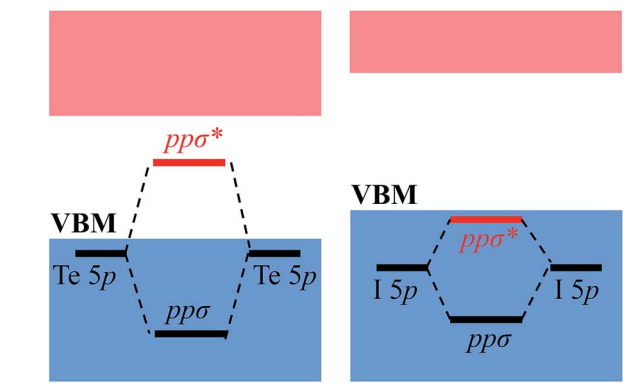

Fig. 11 The schematic diagrams of defect state formation at CdTe and perovskite GBs.

Published on 21 October 2014. Downloaded by ENEA - CASSACCIA on 12/06/2016 17:53:20.

site is even larger. Reduced anion–anion interatomic coupling could partly explain why large cations are necessary in perovskites for high-performance solar cells. It was noted in a previous report[111] that increasing the lattice parameter by applying the tensile strain at the GB of $CuInSe_2$ can effectively push the anion–anion antibonding ppσ* level below the VBM, so that the GB becomes electrically benign. The relatively compact structures of CIS with smaller atoms mean that the wrong bond interactions at GBs are much stronger, creating deep level defects. In perovskites, large atomic sizes and loose crystal structures weaken the wrong bonds at GBs, leading to intrinsically benign GBs.

Ferroelectric effect

Another evident difference between organic–inorganic hybrid perovskites and conventional inorganic absorbers is the dipole moment of the noncentrosymmetric organic cation. Frost *et al.*[56] calculated the electronic dipole of the organic cation in halide perovskites and showed that hybrid perovskites exhibit spontaneous electric polarization, and proposed that the presence of ferroelectric domains will result in internal junctions that may aid electron–hole separation and transportation.

The spontaneous electric polarization in halide perovskites may have two origins. One is the alignment of the dipole moments of organic cations, and the other is intrinsic lattice distortion breaking the crystal centrosymmetry. The calculated magnitude of the $CH_3NH_3PbI_3$ bulk polarization, using the Berry phase method, is 38 $\mu C\ cm^{-2}$, which is comparable to the value of ferroelectric oxide perovskites such as $KNbO_3$ (30 $\mu C\ cm^{-2}$).[56] We note that for ferroelectric perovskite oxide-based solar cells V_{oc} can be larger than the bandgap, and charge separation and carrier lifetime can be enhanced due to the internal electric field.[112]

For halide perovskite-based solar cells, Frost *et al.*[56] proposed that the boundaries of ferroelectric domains may form "ferroelectric highways" that facilitate the transportation of electrons and holes as shown in Fig. 12. Within each domain, where the polarization direction is fixed, electrons and holes can be effectively separated along the direction of the electric field before they can recombine. Crucially, these ferroelectric boundaries are peaks and troughs in electrostatic potential, where electrons and holes automatically choose distinct energetically favorable "highways", avoiding any "collision" with the opposite charge. Such an effect may be another unique property of halide perovskites and a recent experiment[113] claimed direct observation of ferroelectric domains in β phase $CH_3NH_3PbI_3$.

Interface and surface

Although the bulk properties of the absorber are crucial for its solar cell performance, the surface and interface between the absorber, carrier transport layers, and electrode contact layers are also important for efficient carrier transportation. Newly developed growth processes including two-step methods,[8] vacuum deposition, and vapor-assisted solution processing methods,[36] have improved on the quality yielded by the one-step method. These methods improved the uniformity of interfaces and prevented direct contact between hole and electron transportation layers. To further improve the solar cell performance, there are at least three aspects worth consideration.

First is band alignment. The proper band alignments between spiro-MeTAD and perovskites as well as perovskites and TiO_2 make spiro-MeTAD and TiO_2 good candidates for carrier transportation. When photo-excited electrons and holes are generated at CBs and VBs of a perovskite as in Fig. 13, the electrons will move to the CB of TiO_2, while the holes will move to the VBs of the HTM layer. In a dye-sensitized solar cell, the carrier transportations between different layers in solar cells are driven by the band-offset induced electrostatic potential difference near the interfaces. Typical band offsets are schematically shown as Δ_i in Fig. 13. For Δ_1 and Δ_2, overly small band offsets will not facilitate the effective carrier transportation whereas overly large band offsets could reduce the V_{oc}. For Δ_3 and Δ_4, small values are required to avoid further

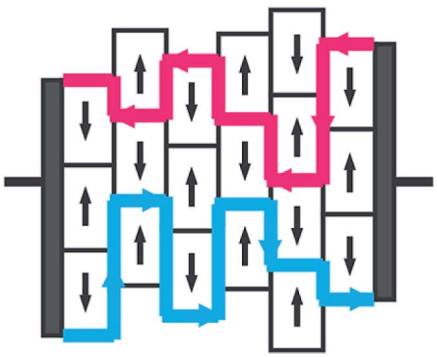

Fig. 12 The schematic diagrams of ferroelectric multidomains as hypothesized in halide perovskite solar cells. The diffusion highways for carriers are indicated by red and blue lines and arrows. Reprinted with permission from ref. 56.

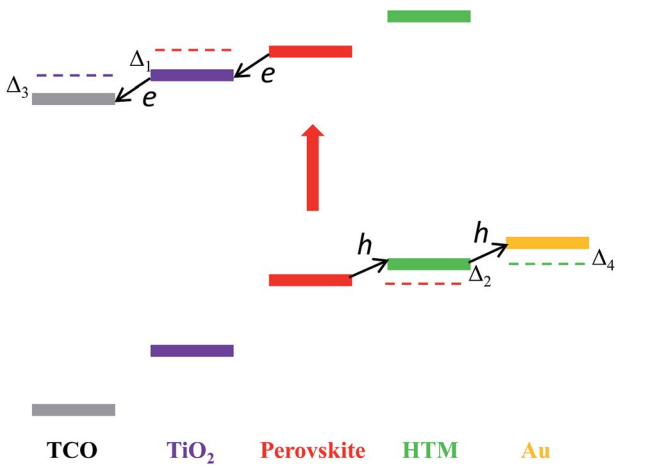

Fig. 13 A schematic band diagram of different functional layers in a perovskite solar cell. The band alignments affecting the cell performance are marked as Δ_i. The band alignments are not to scale and show only the relative positions.

 This journal is © The Royal Society of Chemistry 2015

Published on 21 October 2014. Downloaded by ENEA - CASSACCIA on 12/06/2016 17:53:20.

reduction of V_{oc} while keeping efficient carrier extraction. Recently, Zhou *et al.*[41] optimized the interface by manipulating the interface band alignments. They replaced unintentionally doped TiO_2 with yttrium-doped TiO_2 (Y-TiO_2) and used low work-function ITO to replace high work-function FTO, under the hypothesis that Y-TiO_2 could enhance the electron extraction from perovskites as well as electron transport within TiO_2. This suppressed carrier recombination in the perovskite absorber, facilitated carrier injection into the carrier transport layers, and maintained good carrier extraction at the electrode. As a result, they achieved cell efficiencies up to 19.3%.

The bandgaps and band alignments of perovskites can also be tuned by chemical management of compositional elements, including organic cations,[102,114] Pb,[35,115] and halogen elements.[34,116,117] This is another way to optimize band alignment at interfaces. Currently, the exact energies of band alignments between different layers of materials are unclear. For example, the experimentally reported Δ_1 and Δ_2 values in Fig. 13 are 0.07–0.25 eV and 0.11–0.33 eV, respectively.[32,33,41,91,99,101,118–120] Band alignment calculations are also scarce. First-principles calculations may help identify the optimized materials at interfaces through chemical doping/alloying of oxides or perovskite absorbers.

A second factor is interface structure and passivation. The atomic structures at an interface between two materials with different symmetries are complicated, prone to defects, dangling bonds, and wrong bonds. Those structural deficiencies could introduce deep defect states within bandgap and act as charge traps or recombination centers. The unusual hysteresis of the *I–V* curve of perovskite solar cells,[121,122] which would reduce the working cell efficiency, was suspected to be related to the interface properties. Mosconi *et al.*[54] used first-principles calculations to study the electronic properties of interfaces between TiO_2 and β phase $CH_3NH_3PbI_3$. They found that $CH_3NH_3PbI_3$ tended to grow in a (110)-oriented film on TiO_2, due to better structural matching. Cl was found to enhance the binding energy and thus had stronger modification of interface electronic structure, leading to a stronger interfacial coupling and to a slight TiO_2 CBM upshift. It seems that no deep defect states were found at the TiO_2/$CH_3NH_3PbI_3$ interface, which is consistent with experimental observations that the TiO_2/$CH_3NH_3PbI_3$ interface is more electrically active than the $CH_3NH_3PbI_3$/HTM interface.[110,123] EBIC measurements and surface photovoltage spectroscopy also indicated high electron recombination velocities at this interface. The poor $CH_3NH_3PbI_3$/HTM interface may be why HTM-free perovskite solar cells perform well. Thus, engineering the $CH_3NH_3PbI_3$/HTM interface is crucial, but as of yet there is no theoretical investigation, or available guidelines.

The third factor is surface, which is related to the interface. Abate *et al.*[124] reported the existence of trap states at the perovskite surface, which generated charge accumulation and consequent recombination losses in working solar cells. They identified undercoordinated iodine ions as responsible, and used supramolecular halogen bond complexation for passivation. After passivation, their solar cell demonstrated a maximum power conversion efficiency of 15.7%. On the other hand, the first-principles calculations by Haruyama *et al.*[55] suggested that the electronic structures of various surfaces of β phase $CH_3NH_3PbI_3$, including (110), (001), (100), and (101) surfaces, largely retain the characteristics of bulk $CH_3NH_3PbI_3$. The discrepancies suggest a need for reevaluations of surface properties, both theoretical and experimental. Interestingly, Socampo *et al.*[119] found that the higher cell performance can be achieved by growing tetragonal $CH_3NH_3PbI_3$ with the long axis parallel to the substrate, which can be realized by temperature control during the growth process. This experimental finding is consistent with Mosconi's theoretical prediction of a (110)-oriented perovskite film on TiO_2.[54]

Mixed-halide perovskites

Chemical management of compositional elements[34,35,59,61,101,116,117] has been verified as an effective method for refining the properties of $CH_3NH_3PbI_3$. In general, mixing halides in perovskites has at least three beneficial effects. The first is increasing stability. Lee *et al.*[9] found that perovskite $CH_3NH_3Pb(I_{1-x}Cl_x)_3$ was remarkably stable during processing in air, compared to $CH_3NH_3PbI_3$. Noh *et al.*[34] demonstrated that mixing 20–29% Br into $CH_3NH_3PbI_3$ greatly improved the solar cell stability. The second is enhancing carrier transport. $CH_3NH_3Pb(I_{1-x}Cl_x)_3$ demonstrated much longer electron–hole diffusion length than $CH_3NH_3PbI_3$.[96,97,110,116] Improved carrier mobility and reduced carrier recombination rates were also observed in $CH_3NH_3Pb(I_{1-x}Br_x)_3$ (ref. 125) and $CH_3NH_3Pb(Br_{1-x}Cl_x)_3$.[126] The third is bandgap tuning. $CH_3NH_3PbBr_3$ (ref. 127) ($CH_3NH_3PbBr_{3-x}Cl_x$[126]) has achieved V_{oc} up to 1.3 eV (1.5 eV) and can be used to create colorful solar cell designs for energy-saving buildings. The consecutive bandgap range of mixed halide perovskites $CH_3NH_3Pb(I_{1-x}Cl_x)_3$, $CH_3NH_3Pb(I_{1-x}Br_x)_3$ and $CH_3NH_3Pb(Br_{1-x}Cl_x)_3$ could also be used for application in multi-junction solar cells.[125–127] Solar cells using $CH_3NH_3Pb(I_{1-x}Br_x)_3$ as the light harvester reached 17.9% efficiency in early 2014, the current certified record.[16]

Solar cells using mixed-halide perovskites may potentially achieve efficiencies above 20%. However, there are many fundamental issues that need to be addressed, especially the stability and miscibility between different halide perovskites. For example, the atomic ratio of Cl in $CH_3NH_3PbI(_{1-x}Cl_x)_3$ was previously assumed to be up to one third, as it is in precursors.[9,61] However, recent experiments[76,116] show that its atomic ratio is less than 4% and most of the precursor Cl may be sublimated. Therefore, the miscibility of Cl into iodine should be carefully studied. We used first-principles calculations[128] together with Monte-Carlo simulations based on cluster expansion methods (CEMs)[129,130] to systematically study the structural, electronic, and energetic properties of mixed-halide β phase $CsPbX_3$ (X = I, Br, Cl). The alloy structures were constructed based on special-quasirandom-structure (SQS) within a 160-arom supercell. Computational details have been previously published.[70] The volumes, formation energies, and bandgaps of those SQS alloys generally follow the parabolic shape and their fitting curves are shown in Fig. 14. The

Published on 21 October 2014. Downloaded by ENEA - CASSACCIA on 12/06/2016 17:53:20.

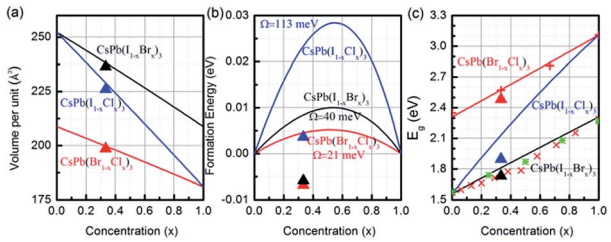

Fig. 14 The (a) volumes, (b) formation energies (per halogen atom), and (c) bandgaps of the mixed halide alloys $CsPbX_{1-x}Y_x$ (X, Y = I, Br, Cl) by SQS calculation. The solid lines are fitted by calculated results of SQS at nine different concentrations (fitted points not shown). The results of the stable ordered structures at $x = 1/3$ are shown as triangles. For bandgaps, the available experimental data are given (red cross marks are from ref. 132, red plus marks are from ref. 34, and green star marks are from ref. 125). The small deviations between experiment and theory may indicate that in the experimental samples the atomic distribution is not perfectly random. Reprinted with permission from ref. 70.

formation energies, ΔH, of alloys in Fig. 14(b) generally follow $\Delta H = \Omega x(1 - x)$. A higher interaction parameter Ω indicates that the alloys are more difficult to form. The calculated Ω values (averaged per halogen atom) for $CsPb(I_{1-x}Cl_x)_3$, $CsPb(I_{1-x}Br_x)_3$, and $CsPb(Br_{1-x}Cl_x)_3$ are 113 meV, 40 meV and 21 meV respectively. The trend of interaction parameters for $CsPb(I_{1-x}Cl_x)_3$, $CsPb(I_{1-x}Br_x)_3$, and $CsPb(Br_{1-x}Cl_x)_3$ follows the trend of ionic size difference between Cl^- (1.67 Å), Br^- (1.84 Å), and I^- (2.07 Å). The miscibility gap temperature at $x = 1/2$, $T_{MG}(x = 1/2)$, can be estimated by $T_{MG} = \Omega/(2k_B)$,[131] where k_B is the Boltzmann constant. In this way, the miscibility gap temperatures of $CsPb(I_{1-x}Cl_x)_3$, $CsPb(I_{1-x}Br_x)_3$, and $CsPb(Br_{1-x}Cl_x)_3$ were calculated to be 625 K, 223 K and 116 K. Since the growth temperature of $CH_3NH_3PbX_3$ is usually below 450 K, our results indicate that mixed-(Br,Cl) and mixed-(I,Br) perovskites could be easily formed, but not mixed-(I,Cl) perovskites. For bandgaps, the experimental results for $CH_3NH_3Pb(I_{1-x}Br_x)_3$ and $CH_3NH_3Pb(Br_{1-x}Cl_x)_3$ are shown in Fig. 14(c), which are overall in agreement with our theoretical calculations. For $CH_3NH_3Pb(I_{1-x}Br_x)_3$, Noh *et al.*[34] observed a bandgap bowing parameter of 0.33 eV. However, Suarez *et al.*[125] found almost zero bandgap bowing, which is close to our theoretical value of −0.01 eV based on SQS.

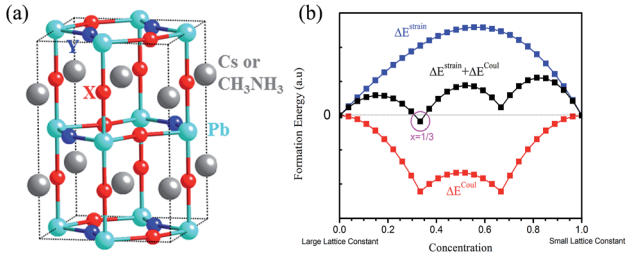

Fig. 15 (a) Our found stable structure at $x = 1/3$. (b) The contributions of strain energy and Coulomb energy in the alloy. Reprinted with permission from ref. 70.

Another interesting finding from our study is a particularly stable alloy structure at $x = 1/3$, where x is the concentration of the perovskite with a smaller lattice constant. Its structure is shown in Fig. 15(a). Monte-Carlo simulations demonstrated that the formation energies of this structure deviate significantly from the parabolic trend and are much lower than in other structures. The unusual stability at $x = 1/3$ may be understood as the combined effect of strain energy and Coulomb energy.

In conventional semiconductor alloys, the formation energies are positive and generally follow $\Delta H = \Omega x(1 - x)$. Such energy mostly comes from the strain energy by which the ideal A and B bulk are stretched or compressed due to the lattice constant of alloy $A_{1-x}B_x$. Usually, a small lattice constant results in a larger bulk modulus, meaning that it is relatively hard to mix large atoms into bulk with a small lattice constant, and easy to mix small atoms into bulk with a large lattice constant. As a result, the maximum value for alloy formation energy is not at $x = 0.5$, but falls closer to the small lattice constant bulk as seen in Fig. 15(b). The formation energies of conventional semiconductor alloys, especially for covalent systems such as $GaAs_{1-x}Sb_x$,[133] follow the strain energies well. However, halide perovskites have strong ionic character, thus Coulomb interactions should play an important role.

For example, consider $CsPb(I_{1-x}Cl_x)_3$. Due to the electronegativity difference between I and Cl, an I electron will partially transfer to Cl, making Cl more negatively charged than I. In this case, the Coulomb energy, modulated by different orders of (I,Cl) structure, could play an important role in total energy. According to cluster expansion methods (CEMs),[129,130] the screened Coulomb energy is approximately proportional to the averaged spin product $\langle\bar{\Pi}(2,1)\rangle$ for anion–anion nearest neighbors. The spin products in CEMs reflect the structural orders in alloys, thus the minimized average spin product $\langle\bar{\Pi}(2,1)\rangle$ in an ionic alloy system corresponds to a particular ordered structure that minimizes the Coulomb energy. Here, the amount of Coulomb energy gain was calculated as the difference between the lowest $\langle\bar{\Pi}(2,1)\rangle$ at particular ordered structures and $\langle\bar{\Pi}(2,1)\rangle$ at random structures at various concentrations. The lowest $\langle\bar{\Pi}(2,1)\rangle$ at ordered structures was derived by minimizing $\langle\bar{\Pi}(2,1)\rangle$ using Monte-Carlo simulations and $\langle\bar{\Pi}(2,1)\rangle$ at random structure was given by $(2x - 1)^2$.[129,130] The calculated Coulomb energy gain is shown in Fig. 15(b). We can see that the alloy system gets the largest Coulomb energy gain at concentration $x = 1/3$ and 2/3. The crystal structure with lowest $\langle\bar{\Pi}(2,1)\rangle$ at $x = 1/3$ is shown in Fig. 15(a), where each Y (blue) ion has maximum (8) nearest neighbors of X (red) anion to minimize $\langle\bar{\Pi}(2,1)\rangle$. In this particular crystal structure, Coulomb energy gain is maximized.

Considering both strain energies and Coulomb energies, we found that the formation energies of mixed halide perovskites had a minimum at $x = 1/3$ (close to the bulk with large lattice constant) as depicted by black lines in Fig. 15(b). Previous DFT–GGA calculations[61] found different stable structure of $CH_3NH_3PbI_2Cl$ where Cl is at the apical site. Here, for the given unit cell, we found that the new structure in Fig. 15(a) is more stable by 60 meV per formula unit than the previous structure. More

 This journal is © The Royal Society of Chemistry 2015

Published on 21 October 2014. Downloaded by ENEA - CASSACCIA on 12/06/2016 17:53:20.

interestingly, the calculated formation energies of $CsPb(I_{2/3}Br_{1/3})_3$, $CsPb(I_{2/3}Cl_{1/3})_3$, and $CsPb(Br_{2/3}Cl_{1/3})_3$ of the new structure were −5 meV, 4 meV, −7 meV per formula unit respectively. Negative formation energies indicate that the perovskite structure can be stabilized by adding halides. Noh *et al.*[34] found that $CH_3NH_3PbI_{3-x}Br_x$-based solar cells exhibit long-term stability at $x = 0.20$ and 0.29, which are close to our prediction of $x = 1/3$ for stable $CsPbI_{3-x}Br_x$. Cl addition into $CH_3NH_3PbI_3$ has also been shown to increase structural stability,[7,9] carrier diffusion length,[96,97,116,125] and solar cell efficiency. Based on our theoretical investigations, we encourage the further study of stabilized mixed-halide perovskites.

Halide perovskites other than $CH_3NH_3PbI_3$

Although most work on perovskites in solar cell applications has focused on $CH_3NH_3PbI_3$, there is an ongoing search for other candidates. Concerns for commercializing $CH_3NH_3PbI_3$ include lead toxicity, a suboptimal bandgap, and long-term stability. Researchers have modified the elemental composition of $CH_3NH_3PbI_3$ to address those concerns.

The reported bandgaps of $CH_3NH_3PbI_3$ are between 1.50 eV and 1.61 eV in the literature. However, the optimal bandgap for a single-junction solar cell is between 1.1 eV and 1.4 eV. Perovskite solar cell efficiencies can be further improved by searching for smaller bandgap perovskites. As discussed, the main role of the cation CH_3NH_3 is stabilizing the perovskite structure. In principle, there are many other choices, such as Cs, NH_4, $C_2H_5NH_3$, and $HC(NH_2)_2$. $CsPbI_3$, NH_4PbI_3 and $C_2H_5NH_3PbI_3$ all have larger bandgaps than $CH_3NH_3PbI_3$. $HC(NH_2)_2PbI_3$ ($FAPbI_3$) has a smaller bandgap of 1.48 eV. $FAPbI_3$-based solar cells have achieved an efficiency of 14.2% and their carrier lifetime is as good as cells using $MAPbI_{3-x}Cl_x$.[99,134] Thermogravimetric measurements on MA- and FA-based perovskites by Hanusch *et al.*[135] indicated that $FAPbI_3$ is more thermally stable than both $MAPbBr_3$ and $MAPbI_3$, which is consistent with the finding that a larger cation at the A site could further stabilize the perovskite structure.

Efforts at making Pb-free perovskites by replacing toxic Pb with other group IVA elements such as Ge and Sn have been attempted. $MASnI_3$ and $CsSnI_3$ can be grown experimentally, and have optimal bandgaps of 1.3 eV.[35,74,77,136,137] Ge-based perovskites such as $CsGeCl_3$ and $MAGeCl_3$ can also be synthesized.[74] However, the stability of the 2+ state decreases from Pb, to Sn, to Ge, which presents a considerable problem. For instance, Sn^{2+} in Sn-based perovskites easily oxidizes to Sn^{4+} in the atmosphere. However, $CH_3NH_3SnI_3$-based solar cells have been made by encapsulating the device under an inert atmosphere, and an efficiency up to 6% has been found,[136,137] demonstrating that Pb-free perovskite solar cells are possible. In addition, a mixed-(Sn,Pb) perovskite, $MAPb_{1-x}Sn_xI_3$, could reduce the amount of used Pb, while tuning the bandgap and retaining the stability.[35,115] The electronic properties and stabilities of Sn-related perovskites and mixed-(Sn,Pb) perovskites should be further studied.

Another possibility is using $MAPbBr_3$ and $MAPbCl_3$, which have larger bandgaps than $MAPbI_3$, as the top layer for tandem perovskite solar cells.[127] $MAPbBr_3$-based solar cells have demonstrated V_{oc} up to 1.5 eV.[126,138] Using a mixed-halide perovskite can tune the bandgap, as well as increase the carrier mobility and structural stability.

Conclusions and prospects

In this paper, the authors review the current understanding of the perovskite materials and their applications in solar cells. First-principles calculations have been proven to be powerful methods for studying the electronic, optical, and defect properties of perovskites, and providing atomistic explanations and guidance for experiments. Theoretical results have demonstrated that halide perovskites exhibit a series of superior electronic and optical properties for solar cell applications, such as proper bandgap and band alignment, high optical absorption, bipolar carrier conductivity, tunable doping ability, and benign defect properties.

Theoretical studies can address a number of other aspects of perovskites' behavior in solar applications. One is anomalous hysteresis in perovskite solar cells.[122] Frost *et al.*[52] have proposed that the dipole moment of organic cations could contribute to the hysteresis, although recent experiments suggested that grain sizes and interface may play an important role,[139] which requires further investigation. Further first-principles investigations are needed to optimize the material's properties, and to find new perovskite candidates for high-efficiency, stable solar cells. As previously mentioned, the bandgap of archetypal halide perovskite $CH_3NH_3PbI_3$ is larger than the ideal. Band structure engineering of $CH_3NH_3PbI_3$ could be extensively investigated by replacing organic cations, Pb, or I with other choices. Furthermore, the mechanisms of performance degradations are still not well studied, even though long-term stability is a crucial aspect of commercialization. Rapid degradation in moist environments has suggested that water may corrode perovskites. The chemical reactions between H_2O and the perovskite surface could be carefully studied to unravel the reaction mechanism, leading to the development of methods for stabilizing perovskites. Long-term stable perovskite solar cells have recently been fabricated in the laboratory through chemical composition engineering.[34,101,114] However, the fundamental reason for alloy stabilization of the structures requires more study. Overall, first-principles calculations will continue to play an important role in the understanding and development of the emerging technology of perovskite solar cells.

Acknowledgements

This research was funded by the U.S. Department of Energy under Grant no. DE-AC36-08GO28308 with the National Renewable Energy Laboratory. Funding for the work was provided by the DOE Office of Energy Efficiency and Renewable Energy. This work used the NREL Peregrine Supercomputer, the Ohio Supercomputer Center and the National Energy Research

Published on 21 October 2014. Downloaded by ENEA - CASSACCIA on 12/06/2016 17:53:20.

Scientific Computing Center, which is supported by the Office of Science of the U.S. Department of Energy under Contract no. DE-AC02-05CH11231. Y.Y. acknowledges the support of the Ohio Research Scholar Program.

Notes and references

1 R. E. Cohen, *Nature*, 1992, **358**, 136–138.
2 M. A. Pena and J. L. G. Fierro, *Chem. Rev.*, 2001, **101**, 1981–2017.
3 P. Gao, M. Grätzel and M. K. Nazeeruddin, *Energy Environ. Sci.*, 2014, **7**, 2448–2463.
4 S. A. Bretschneider, J. Weickert, J. A. Dorman and L. Schmidt-Mende, *APL Mater.*, 2014, **2**, 040701.
5 H. J. Snaith, *J. Phys. Chem. Lett.*, 2013, **4**, 3623–3630.
6 N.-G. Park, *J. Phys. Chem. Lett.*, 2013, **4**, 2423–2429.
7 M. Liu, M. B. Johnston and H. J. Snaith, *Nature*, 2013, **501**, 395–398.
8 J. Burschka, N. Pellet, S.-J. Moon, R. Humphry-Baker, P. Gao, M. K. Nazeeruddin and M. Grätzel, *Nature*, 2013, **499**, 316–319.
9 M. M. Lee, J. Teuscher, T. Miyasaka, T. N. Murakami and H. J. Snaith, *Science*, 2012, **338**, 643–647.
10 I. Chung, B. Lee, J. He, R. P. H. Chang and M. G. Kanatzidis, *Nature*, 2012, **485**, 486–U494.
11 A. Kojima, K. Teshima, Y. Shirai and T. Miyasaka, *J. Am. Chem. Soc.*, 2009, **131**, 6050–6051.
12 N.-G. Park, *Mater. Today*, 2014, DOI: 10.1016/j.mattod.2014.07.007.
13 M. A. Green, A. Ho-Baillie and H. J. Snaith, *Nat. Photonics*, 2014, **8**, 506–514.
14 M. Grätzel, *Nat. Mater.*, 2014, **13**, 838–842.
15 M. D. McGehee, *Nat. Mater.*, 2014, **13**, 845–846.
16 http://www.nrel.gov/ncpv/images/efficiency_chart.jpg.
17 H.-S. Kim, C.-R. Lee, J.-H. Im, K.-B. Lee, T. Moehl, A. Marchioro, S.-J. Moon, R. Humphry-Baker, J.-H. Yum, J. E. Moser, M. Grätzel and N.-G. Park, *Sci. Rep.*, 2012, **2**, 591.
18 H. L. Z. Wells, *Anorg. Chem.*, 1893, **3**, 195.
19 K. Yamada, K. Isobe, E. Tsuyama, T. Okuda and Y. Furukawa, *Solid State Ionics*, 1995, **79**, 152–157.
20 W. Depmeier, A. Moller and K. H. Klaska, *Acta Crystallogr., Sect. B: Struct. Sci.*, 1980, **36**, 803–807.
21 B. Winkler, V. Milman and M. H. Lee, *J. Chem. Phys.*, 1998, **108**, 5506–5509.
22 C. K. Moller, *Nature*, 1958, **182**, 1436.
23 A. N. R. S. E. Christensen, *Acta Chem. Scand.*, 1965, **19**, 421.
24 C. K. Moller, *Nature*, 1957, **180**, 981.
25 D. Weber, *Z. Naturforsch., B: Anorg. Chem., Org. Chem.*, 1978, **33**, 1443.
26 D. B. Mitzi, K. Chondroudis and C. R. Kagan, *IBM J. Res. Dev.*, 2001, **45**, 29–45.
27 D. B. Mitzi, *J. Chem. Soc., Dalton Trans.*, 2001, **1**, 1–12.
28 D. B. Mitzi, *Chem. Mater.*, 2001, **13**, 3283–3298.
29 D. B. Mitzi, S. Wang, C. A. Feild, C. A. Chess and A. M. Guloy, *Science*, 1995, **267**, 1473–1476.
30 Z.-K. Tan, R. S. Moghaddam, M. L. Lai, P. Docampo, R. Higler, F. Deschler, M. Price, A. Sadhanala, L. M. Pazos, D. Credgington, F. Hanusch, T. Bein, H. J. Snaith and R. H. Friend, *Nat. Nanotechnol.*, 2014, **9**, 687–692.
31 A. T. Kojima, K. Teshima and Y. Shirai, *Proc. 210th ECS Meeting (ECS, 2006)*, 2006, abstract #397.
32 J.-H. Im, C.-R. Lee, J.-W. Lee, S.-W. Park and N.-G. Park, *Nanoscale*, 2011, **3**, 4088–4093.
33 N. J. Jeon, J. H. Noh, Y. C. Kim, W. S. Yang, S. Tyu and S. I. Seok, *Nat. Mater.*, 2014, **13**, 897–903.
34 J. H. Noh, S. H. Im, J. H. Heo, T. N. Mandal and S. I. Seok, *Nano Lett.*, 2013, **13**, 1764–1769.
35 Y. Ogomi, A. Morita, S. Tsukamoto, T. Saitho, N. Fujikawa, Q. Shen, T. Toyoda, K. Yoshino, S. S. Pandey, T. L. Ma and S. Hayase, *J. Phys. Chem. Lett.*, 2014, **5**, 1004–1011.
36 Q. Chen, H. P. Zhou, Z. R. Hong, S. Luo, H. S. Duan, H. H. Wang, Y. S. Liu, G. Li and Y. Yang, *J. Am. Chem. Soc.*, 2014, **136**, 622–625.
37 J. J. Shi, Y. H. Luo, H. Y. Wei, J. H. Luo, J. Dong, S. T. Lv, J. Y. Xiao, Y. Z. Xu, L. F. Zhu, X. Xu, H. J. Wu, D. M. Li and Q. B. Meng, *ACS Appl. Mater. Interfaces*, 2014, **6**, 9711–9718.
38 N. J. Jeon, J. Lee, J. H. Noh, M. K. Nazeeruddin, M. Grätzel and S. I. Seok, *J. Am. Chem. Soc.*, 2013, **135**, 19087–19090.
39 N. J. Jeon, H. G. Lee, Y. C. Kim, J. Seo, J. H. Noh, J. Lee and S. I. Seok, *J. Am. Chem. Soc.*, 2014, **136**, 7837–7840.
40 D. Q. Bi, L. Yang, G. Boschloo, A. Hagfeldt and E. M. J. Johansson, *J. Phys. Chem. Lett.*, 2013, **4**, 1532–1536.
41 H. P. Zhou, Q. Chen, G. Li, S. Luo, T. B. Song, H. S. Duan, Z. R. Hong, J. B. You, Y. S. Liu and Y. Yang, *Science*, 2014, **345**, 542–546.
42 Q. Chen, H. P. Zhou, T. B. Song, S. Luo, Z. R. Hong, H. S. Duan, L. T. Dou, Y. S. Liu and Y. Yang, *Nano Lett.*, 2014, **14**, 4158–4163.
43 W. Shockley and H. J. Queisser, *J. Appl. Phys.*, 1961, **32**, 510.
44 Y. H. Chang, C. H. Park and K. Matsuishi, *J. Korean Phys. Soc.*, 2004, **44**, 889–893.
45 I. Borriello, G. Cantele and D. Ninno, *Phys. Rev. B: Condens. Matter Mater. Phys.*, 2008, **77**, 235214.
46 Y. Wang, T. Gould, J. F. Dobson, H. M. Zhang, H. G. Yang, X. D. Yao and H. J. Zhao, *Phys. Chem. Chem. Phys.*, 2014, **16**, 1424–1429.
47 J. C. Menendez-Proupin, E. Palacios, P. Wahnon and P. Conesa, *Phys. Rev. B: Condens. Matter Mater. Phys.*, 2014, **90**, 045207.
48 R. Gottesman, E. Haltzi, L. Gouda, S. Tirosh, Y. Bouhadana and A. Zaban, *J. Phys. Chem. Lett.*, 2014, **5**, 2662–2669.
49 G. Murtaza, I. Ahmad, M. Maqbool, H. A. R. Aliabad and A. Afaq, *Chin. Phys. Lett.*, 2011, **28**, 117803.
50 G. Murtaza and I. Ahmad, *Physica B*, 2011, **406**, 3222–3229.
51 X. Zhu, H. Su, R. A. Marcus and M. E. Michel-Beyerle, *J. Phys. Chem. Lett.*, 2014, **5**, 3061.
52 F. Brivio, A. B. Walker and A. Walsh, *APL Mater.*, 2014, **2**, 081506.
53 T. Minemoto and M. Murata, *J. Appl. Phys.*, 2014, **116**, 054505.
54 E. Mosconi, E. Ronca and F. De Angelis, *J. Phys. Chem. Lett.*, 2014, **5**, 2619–2625.

 This journal is © The Royal Society of Chemistry 2015

Published on 21 October 2014. Downloaded by ENEA - CASSACCIA on 12/06/2016 17:53:20.

55 J. S. Haruyama, K. Sodeyama, L. Han and Y. Tateyama, *J. Phys. Chem. Lett.*, 2014, **5**, 2903–2909.
56 K. T. B. Jarvist, M. Frost, F. Brivio, C. H. Hendon, M. van Schilfgaarde and A. Walsh, *Nano Lett.*, 2014, **14**, 2584.
57 F. Brivio, K. T. Butler, A. Walsh and M. van Schilfgaarde, *Phys. Rev. B: Condens. Matter Mater. Phys.*, 2014, **89**, 155204.
58 F. Brivio, A. B. Walker and A. Walsh, *APL Mater.*, 2013, **1**, 042111.
59 A. Amat, E. Mosconi, E. Ronca, C. Quarti, P. Umari, M. K. Nazeeruddin, M. Grätzel and F. De Angelis, *Nano Lett.*, 2014, **14**, 3608–3616.
60 P. Umari, E. Mosconi and F. De Angelis, *Sci. Rep.*, 2014, **4**, 4464.
61 E. Mosconi, A. Amat, M. K. Nazeeruddin, M. Grätzel and F. De Angelis, *J. Phys. Chem. C*, 2013, **117**, 13902–13913.
62 W.-J. Yin, T. Shi and Y. Yan, *Adv. Mater.*, 2014, **26**, 4653–4658.
63 W. J. Yin, T. Shi and Y. Yan, *Appl. Phys. Lett.*, 2014, **104**, 063903.
64 J. Kim, S. H. Lee, J. H. Lee and K. H. Hong, *J. Phys. Chem. Lett.*, 2014, **5**, 1312–1317.
65 G. Giorgi, J. I. Fujisawa, H. Segawa and K. Yamashita, *J. Phys. Chem. Lett.*, 2013, **4**, 4213–4216.
66 J. Even, L. Pedesseau, J. M. Jancu and C. Katan, *J. Phys. Chem. Lett.*, 2013, **4**, 2999–3005.
67 A. Filippetti and A. Mattoni, *Phys. Rev. B: Condens. Matter Mater. Phys.*, 2014, **89**, 125203.
68 L. Lang, J. H. Yang, H. R. Liu, H. J. Xiang and X. G. Gong, *Phys. Lett. A*, 2014, **378**, 290–293.
69 W.-J. Yin, H. Y. Chen, T. Shi, S.-H. Wei, and Y. Yan, unpublished.
70 W.-J. Yin, Y. Yan and S.-H. Wei, *J. Phys. Chem. Lett.*, 2014, **5**, 3625–3631.
71 D. A. Egger and L. Kronik, *J. Phys. Chem. Lett.*, 2014, **5**, 2728–2733.
72 J. Miller, *Phys. Today*, 2014, **67**, 13.
73 C. H. Li, X. G. Lu, W. Z. Ding, L. M. Feng, Y. H. Gao and Z. G. Guo, *Acta Crystallogr., Sect. B: Struct. Sci.*, 2008, **64**, 702–707.
74 T. Baikie, Y. N. Fang, J. M. Kadro, M. Schreyer, F. X. Wei, S. G. Mhaisalkar, M. Grätzel and T. J. White, *J. Mater. Chem. A*, 2013, **1**, 5628–5641.
75 C. C. Stoumpos, C. D. Malliakas and M. G. Kanatzidis, *Inorg. Chem.*, 2013, **52**, 9019–9038.
76 J. M. Ball, M. M. Lee, A. Hey and H. J. Snaith, *Energy Environ. Sci.*, 2013, **6**, 1739–1743.
77 I. Chung, J. H. Song, J. Im, J. Androulakis, C. D. Malliakas, H. Li, A. J. Freeman, J. T. Kenney and M. G. Kanatzidis, *J. Am. Chem. Soc.*, 2012, **134**, 8579–8587.
78 A. Walsh and G. W. Watson, *J. Solid State Chem.*, 2005, **178**, 1422–1428.
79 A. Walsh, D. J. Payne, R. G. Egdell and G. W. Watson, *Chem. Soc. Rev.*, 2011, **40**, 4455–4463.
80 S. H. Wei and A. Zunger, *Phys. Rev. B: Condens. Matter Mater. Phys.*, 1997, **55**, 13605–13610.
81 M. H. Du, *J. Mater. Chem. A*, 2014, **2**, 9091–9098.
82 H. J. Zhang, C. X. Liu, X. L. Qi, X. Dai, Z. Fang and S. C. Zhang, *Nat. Phys.*, 2009, **5**, 438–442.
83 L. P. Yu and A. Zunger, *Phys. Rev. Lett.*, 2012, **108**, 068701.
84 L. P. Yu, R. S. Kokenyesi, D. A. Keszler and A. Zunger, *Adv. Energy Mater.*, 2013, **3**, 43–48.
85 M. A. Green, K. Emery, Y. Hishikawa, W. Warta and E. D. Dunlop, *Prog. Photovoltaics*, 2014, **22**, 701–710.
86 A. Polizzotti, I. L. Repins, R. Noufi, S. H. Wei and D. B. Mitzi, *Energy Environ. Sci.*, 2013, **6**, 3171–3182.
87 S. Y. Chen, J. H. Yang, X. G. Gong, A. Walsh and S. H. Wei, *Phys. Rev. B: Condens. Matter Mater. Phys.*, 2010, **81**, 245204.
88 Y. X. Zhao, A. M. Nardes and K. Zhu, *J. Phys. Chem. Lett.*, 2014, **5**, 490–494.
89 C. S. Ponseca, T. J. Savenije, M. Abdellah, K. B. Zheng, A. Yartsev, T. Pascher, T. Harlang, P. Chabera, T. Pullerits, A. Stepanov, J. P. Wolf and V. Sundstrom, *J. Am. Chem. Soc.*, 2014, **136**, 5189–5192.
90 L. Etgar, P. Gao, Z. Xue, Q. Peng, A. K. Chandiran, B. Liu, M. K. Nazeeruddin and M. Grätzel, *J. Am. Chem. Soc.*, 2012, **134**, 17396–17399.
91 W. Abu Laban and L. Etgar, *Energy Environ. Sci.*, 2013, **6**, 3249–3253.
92 J. B. You, Z. R. Hong, Y. Yang, Q. Chen, M. Cai, T. B. Song, C. C. Chen, S. R. Lu, Y. S. Liu, H. P. Zhou and Y. Yang, *ACS Nano*, 2014, **8**, 1674–1680.
93 S. B. Zhang, S. H. Wei, A. Zunger and H. Katayama-Yoshida, *Phys. Rev. B: Condens. Matter Mater. Phys.*, 1998, **57**, 9642–9656.
94 S. Y. Chen, X. G. Gong, A. Walsh and S. H. Wei, *Appl. Phys. Lett.*, 2009, **94**, 041903.
95 W. J. Yin, S. H. Wei, M. M. Al-Jassim and Y. F. Yan, *Appl. Phys. Lett.*, 2011, **99**, 142109.
96 G. C. Xing, N. Mathews, S. Y. Sun, S. S. Lim, Y. M. Lam, M. Grätzel, S. Mhaisalkar and T. C. Sum, *Science*, 2013, **342**, 344–347.
97 S. D. Stranks, G. E. Eperon, G. Grancini, C. Menelaou, M. J. P. Alcocer, T. Leijtens, L. M. Herz, A. Petrozza and H. J. Snaith, *Science*, 2013, **342**, 341–344.
98 A. S. Subbiah, A. Halder, S. Ghosh, N. Mahuli, G. Hodes and S. K. Sarkar, *J. Phys. Chem. Lett.*, 2014, **5**, 1748–1753.
99 P. Qin, S. Tanaka, S. Ito, N. Tetreault, K. Manabe, H. Nishino, M. K. Nazeeruddin and M. Grätzel, *Nat. Commun.*, 2014, **5**, 3834.
100 J. A. Christians, R. C. M. Fung and P. V. Kamat, *J. Am. Chem. Soc.*, 2014, **136**, 758–764.
101 A. Mei, L. Liu, Z. Ku, T. Liu, Y. Rong, M. Xu, M. Hu, J. Chen, Y. Yang, M. Grätzel and H. Han, *Science*, 2014, **345**, 295–298.
102 J. J. Shi, J. Dong, S. T. Lv, Y. Z. Xu, L. F. Zhu, J. Y. Xiao, X. Xu, H. J. Wu, D. M. Li, Y. H. Luo and Q. B. Meng, *Appl. Phys. Lett.*, 2014, **104**, 063901.
103 S. Aharon, B. El Cohen and L. Etgar, *J. Phys. Chem. C*, 2014, **118**, 17160–17165.
104 M. L. Agiorgousis, Y.-Y. Sun, H. Zeng and S. Zhang, *J. Am. Chem. Soc.*, 2014, **136**, 14570–14575.
105 J. J. Choi, X. H. Yang, Z. M. Norman, S. J. L. Billinge and J. S. Owen, *Nano Lett.*, 2014, **14**, 127–133.
106 C. Li, Y. L. Wu, J. Poplawsky, T. J. Pennycook, N. Paudel, W. J. Yin, S. J. Haigh, M. P. Oxley, A. R. Lupini, M. Al-

Published on 21 October 2014. Downloaded by ENEA - CASSACCIA on 12/06/2016 17:53:20.

Jassim, S. J. Pennycook and Y. F. Yan, *Phys. Rev. Lett.*, 2014, **112**, 156103.
107 C. B. Feng, W. J. Yin, J. L. Nie, X. T. Zu, M. N. Huda, S. H. Wei, M. M. Al-Jassim and Y. F. Yon, *Solid State Commun.*, 2012, **152**, 1744–1747.
108 W. J. Yin, Y. L. Wu, R. Noufi, M. Al-Jassim and Y. F. Yan, *Appl. Phys. Lett.*, 2013, **102**, 193905.
109 W. J. Yin, Y. L. Wu, S. H. Wei, R. Noufi, M. M. Al-Jassim and Y. F. Yan, *Adv. Energy Mater.*, 2014, **4**, 1300712.
110 E. Edri, S. Kirmayer, A. Henning, S. Mukhopadhyay, K. Gartsman, Y. Rosenwaks, G. Hodes and D. Cahen, *Nano Lett.*, 2014, **14**, 1000–1004.
111 Y. Yan, C. S. Jiang, R. Noufi, S. H. Wei, H. R. Moutinho and M. M. Al-Jassim, *Phys. Rev. Lett.*, 2007, **99**, 235504.
112 I. Grinberg, D. V. West, M. Torres, G. Y. Gou, D. M. Stein, L. Y. Wu, G. N. Chen, E. M. Gallo, A. R. Akbashev, P. K. Davies, J. E. Spanier and A. M. Rappe, *Nature*, 2013, **503**, 509–512.
113 Y. Kutes, L. Ye, Y. Zhou, S. Pang, B. D. Huey and N. P. Padture, *J. Phys. Chem. Lett.*, 2014, **5**, 3335–3339.
114 N. Pellet, P. Gao, G. Gregori, T. Y. Yang, M. K. Nazeeruddin, J. Maier and M. Grätzel, *Angew. Chem., Int. Ed.*, 2014, **53**, 3151–3157.
115 F. Hao, C. C. Stoumpos, R. P. H. Chang and M. G. Kanatzidis, *J. Am. Chem. Soc.*, 2014, **136**, 8094–8099.
116 S. Colella, E. Mosconi, P. Fedeli, A. Listorti, F. Gazza, F. Orlandi, P. Ferro, T. Besagni, A. Rizzo, G. Calestani, G. Gigli, F. De Angelis and R. Mosca, *Chem. Mater.*, 2013, **25**, 4613–4618.
117 S. A. Kulkarni, T. Baikie, P. P. Boix, N. Yantara, N. Mathews and S. Mhaisalkar, *J. Mater. Chem. A*, 2014, **2**, 9221–9225.
118 J. H. Noh, N. J. Jeon, Y. C. Choi, M. K. Nazeeruddin, M. Grätzel and S. I. Seok, *J. Mater. Chem. A*, 2013, **1**, 11842–11847.
119 P. Docampo, F. C. Hanusch, N. Giesbrecht, P. Angloher, A. Ivanova and T. Bein, *APL Mater.*, 2014, **2**, 081508.
120 Y. G. Rong, Z. L. Ku, A. Y. Mei, T. F. Liu, M. Xu, S. G. Ko, X. Li and H. W. Han, *J. Phys. Chem. Lett.*, 2014, **5**, 2160–2164.
121 R. S. Sanchez, V. Gonzalez-Pedro, J. W. Lee, N. G. Park, Y. S. Kang, I. Mora-Sero and J. Bisquert, *J. Phys. Chem. Lett.*, 2014, **5**, 2357–2363.
122 H. J. Snaith, A. Abate, J. M. Ball, G. E. Eperon, T. Leijtens, N. K. Noel, S. D. Stranks, J. T. W. Wang, K. Wojciechowski and W. Zhang, *J. Phys. Chem. Lett.*, 2014, **5**, 1511–1515.
123 E. Edri, S. Kirmayer, S. Mukhopadhyay, K. Gartsman, G. Hodes and D. Cahen, *Nat. Commun.*, 2014, **5**, 3461.
124 A. Abate, M. Saliba, D. J. Hollman, S. D. Stranks, K. Wojciechowski, R. Avolio, G. Grancini, A. Petrozza and H. J. Snaith, *Nano Lett.*, 2014, **14**, 3247–3254.
125 B. Suarez, V. Gonzalez-Pedro, T. S. Ripolles, R. S. Sanchez, L. Otero and I. Mora-Sero, *J. Phys. Chem. Lett.*, 2014, **5**, 1628–1635.
126 E. Edri, S. Kirmayer, M. Kulbak, G. Hodes and D. Cahen, *J. Phys. Chem. Lett.*, 2014, **5**, 429–433.
127 E. Edri, S. Kirmayer, D. Cahen and G. Hodes, *J. Phys. Chem. Lett.*, 2013, **4**, 897–902.
128 G. Kresse and J. Furthmuller, *Phys. Rev. B: Condens. Matter Mater. Phys.*, 1996, **54**, 11169–11186.
129 A. Zunger, S. H. Wei, L. G. Ferreira and J. E. Bernard, *Phys. Rev. Lett.*, 1990, **65**, 353–356.
130 S. H. Wei, L. G. Ferreira, J. E. Bernard and A. Zunger, *Phys. Rev. B: Condens. Matter Mater. Phys.*, 1990, **42**, 9622–9649.
131 S. H. Wei, L. G. Ferreira and A. Zunger, *Phys. Rev. B: Condens. Matter Mater. Phys.*, 1990, **41**, 8240–8269.
132 N. Kitazawa, Y. Watanabe and Y. Nakamura, *J. Mater. Sci.*, 2002, **37**, 3585–3587.
133 L. G. Ferreira, S. H. Wei and A. Zunger, *Phys. Rev. B: Condens. Matter Mater. Phys.*, 1989, **40**, 3197–3231.
134 G. E. Eperon, S. D. Stranks, C. Menelaou, M. B. Johnston, L. M. Herz and H. J. Snaith, *Energy Environ. Sci.*, 2014, **7**, 982–988.
135 F. C. Hanusch, E. Wiesenmayer, E. Mankel, A. Binek, P. Angloher, C. Fraunhofer, N. Giesbrecht, J. M. Feckl, W. Jaegermann, D. Johrendt, T. Bien and P. Docampo, *J. Phys. Chem. Lett.*, 2014, **5**, 2791.
136 F. Hao, C. C. Stoumpos, D. H. Cao, R. P. H. Chang and M. G. Kanatzidis, *Nat. Photonics*, 2014, **8**, 489–494.
137 N. K. Noel, S. D. Stranks, A. Abate, C. Wehrenfennig, S. Guarnera, A. A. Haghighirad, A. Sadhanala, G. E. Eperson, M. B. Johnston, A. M. Petrozza, L. M. Herz and H. J. Snaith, *Energy Environ. Sci.*, 2014, **7**, 3061.
138 M. Zhang, H. Yu, M. Lyu, Q. Wang, J.-H. Yun and L. Wang, *Chem. Commun.*, 2014, **50**, 11727–11730.
139 E. L. Unger, E. T. Hoke, C. D. Bailie, W. H. Nguyen, A. R. Bowring, T. Heumuller, M. G. Christoforo and M. D. McGehee, *Energy Environ. Sci.*, 2014, **7**, 3690–3698.

 This journal is © The Royal Society of Chemistry 2015